

Mechanisms of inward transmembrane proton translocation

Kirill Kovalev, Fedor Tsybrov, Alexey Alekseev, Vitaly Shevchenko, Dmytro Soloviov, Sergey Siletsky, Gleb Bourenkov, Michael Agthe, Marina Nikolova, David von Stetten, et al.

▶ To cite this version:

Kirill Kovalev, Fedor Tsybrov, Alexey Alekseev, Vitaly Shevchenko, Dmytro Soloviov, et al.. Mechanisms of inward transmembrane proton translocation. Nature Structural and Molecular Biology, 2023, 30 (7), pp.970-979. 10.1038/s41594-023-01020-9. hal-04216521

HAL Id: hal-04216521

https://hal.science/hal-04216521

Submitted on 25 Nov 2023

HAL is a multi-disciplinary open access archive for the deposit and dissemination of scientific research documents, whether they are published or not. The documents may come from teaching and research institutions in France or abroad, or from public or private research centers.

L'archive ouverte pluridisciplinaire **HAL**, est destinée au dépôt et à la diffusion de documents scientifiques de niveau recherche, publiés ou non, émanant des établissements d'enseignement et de recherche français ou étrangers, des laboratoires publics ou privés.

21 3. Source Data

Parent Figure or Table	Filename Whole original file name including extension. i.e.: Smith_SourceData_Fig1.xls, or Smith_ Unmodified_Gels_Fig1.pdf	Data description i.e.: Unprocessed western Blots and/or gels, Statistical Source Data, etc.
Source Data Fig. 1	Fig1.xlsx	Experimental Source Data
Source Data Fig. 2	Fig2.xlsx	Experimental Source Data
Source Data Extended Data Fig./Table 1	Ext1.xlsx	Experimental Source Data
Source Data Extended Data Fig./Table 2	Ext2.xlsx	Experimental Source Data
Source Data Extended Data Fig./Table 5	Ext5.xlsx	Experimental Source Data

2223

Title: Mechanisms of inward transmembrane proton translocation

25

24

- 26 **Author list:** K. Kovalev^{1*}, F. Tsybrov^{2*}, A. Alekseev^{2,3*}, V. Shevchenko², D. Soloviov¹, S. Siletsky⁴, G.
- 27 Bourenkov¹, M. Agthe¹, M. Nikolova¹, D. von Stetten¹, R. Astashkin⁵, S. Bukhdruker², I. Chizhov⁶, A.
- Royant⁵, A. Kuzmin², I. Gushchin², R. Rosselli⁷, F. Rodriguez-Valera^{2,8}, N. Ilyinskiy², A. Rogachev^{2,9}, V.
- 29 Borshchevskiy^{2,9}, T. R. Schneider¹, E. Bamberg¹⁰, V. Gordeliy^{2,5#}.

30

31 Affiliations:

- 32 ¹ European Molecular Biology Laboratory, Hamburg unit c/o DESY, Hamburg, Germany
- ² Research Center for Molecular Mechanisms of Aging and Age-Related Diseases, Moscow Institute of
- 34 Physics and Technology, Dolgoprudny, Russia
- 35 ³ Institute for Auditory Neuroscience and InnerEarLab, University Medical Center Göttingen, Göttingen,
- 36 Germany
- ⁴ Belozersky Institute of Physical-Chemical Biology, Lomonosov Moscow State University, Moscow,
- 38 Russian Federation
- ⁵ Univ. Grenoble Alpes, CEA, CNRS, Institut de Biologie Structurale (IBS), 38000 Grenoble, France
- 40 ⁶ Institute for Biophysical Chemistry, Hannover Medical School, Germany
- ⁷ Dpto. Fisiología, Genética y Microbiología, Universidad de Alicante, Alicante, Spain
- 42 8 Evolutionary Genomics Group, Departamento de Produccion Vegetal y Microbiologia, Universidad
- 43 Miguel Hernandez, San Juan de Alicante, Alicante, Spain
- ⁹ Joint Institute for Nuclear Research, Dubna 141980, Russian Federation
- 45 ¹⁰ Max Planck Institute of Biophysics, Frankfurt am Main, Germany

- * These authors contributed equally to the work.
- 48 #Correspondence to: V.G. (valentin.gordeliy@gmail.com)

Abstract

Proton transport is indispensable for cell life. It is believed that molecular mechanisms of proton movement through different types of proton-conducting molecules have general universal features. However, elucidation of such mechanisms is a challenge. It requires true-atomic-resolution structures of all key proton conducting states. Here we present a comprehensive function-structure study of a light-driven bacterial inward proton pump xenorhodopsin from *Bacillus coahuilensis* in all major proton conducting states. The structures reveal that proton translocation is based on proton wires regulated by internal gates. The wires serve as both selectivity filters and translocation pathways for protons. The cumulative results suggest a general concept of proton translocation. We demonstrate the use of serial time-resolved crystallography at a synchrotron source with sub-millisecond resolution for rhodopsin studies opening the door for principally new applications. The results might also be of interest for optogenetics since xenorhodopsins are the only alternative tools to fire neurons.

Main text

64

63

- Ion gradients across cell membranes are crucial for life and are maintained by ion transporters. Proton transporters are in the focus of studies of molecular mechanisms of ion transport. In many microorganisms from all domains of life proton gradients are maintained by membrane hepta-α-helical light-driven proteins -
- 68 microbial rhodopsins (MRs) comprising a retinal as a chromophore¹. The most studied proton-transporting
- 69 MRs are light-driven outward pumps serving as a reference for the understanding of proton transfer and
- storage in proteins².
- Moreover, MRs found their principal application in optogenetics, which revolutionized neuroscience and
- offered novel biomedical approaches; recently it was used for partial vision recovery in humans³. Mostly
- 73 cation channelrhodopsins (CCRs) are employed for optical activation of cells. Starting in 2016, the first
- inwardly-directed proton pumps (IPPs) xenorhodopsins (XeRs) were found and characterized⁴⁻⁶. IPPs are the
- only alternative optogenetic instruments to CCRs affording a set of competitive advantages⁶. However, the
- optimization of XeRs (and IPPs in general) is essential for optogenetics due to their slow kinetics resulting in
- insufficient photocurrents for routine usage^{4,7}. High-resolution insights into the mechanisms of XeRs
- 78 functioning are imperative for their rational optimization.
- 79 Unfortunately, the molecular mechanism of inward proton translocation remains unclear. It is believed that
- 80 upon light illumination the retinal Schiff base (RSB) of XeR donates its proton to the internal proton acceptor
- located in the cytoplasmic part of the protein^{4,6}. This transfer coincides with the formation of the strongly
- 82 blue-shifted M intermediate, which then decays with the protein returning back to its ground state
- accompanied by a proton release to the cytoplasm and a proton uptake from the extracellular bulk⁴⁻⁶. However,
- 84 there is no certain information on the internal proton transfer and also on the determinants of inwardly-directed
- 85 proton translocation.
- 86 In this work, we found a bacterial xenorhodopsin from *Bacillus coahuilensis* (*Bc*XeR), which is an ideal target
- 87 to reveal the molecular mechanism of inward proton translocation. We used time-resolved serial
- crystallography at the P14 beamline of the PETRAIII synchrotron source with time resolution up to 500 µs to
- 89 capture the structural rearrangements in BcXeR during the photocycle. Moreover, X-ray data on the
- 90 cryotrapped intermediates allowed us to build more detailed models of the ground, L, and M states at 1.6-1.7
- A resolution to visualize water-mediated proton wires inside BcXeR acting as pathways for unidirectional
- 92 proton translocation. We validated our structural findings by functional and spectroscopic studies of the
- 93 protein and its mutant forms. Based on the described data we propose a molecular mechanism of the light-
- 94 driven inward proton translocation also serving as a unique reference for understanding of the proton transport
- 95 in general.

96

The gene encoding *Bc*XeR was identified bioinformatically in GenBank (ID: WP_059282687) using Hidden Markov Model algorithms (see Methods for details). The protein is a member of the bacterial XeR clade and could be easily expressed in *E.coli* with high yield (Extended Data Fig. 1). The same gene was previously predicted to encode a sensory rhodopsin⁸. However, *Bc*XeR-expressing *E.coli* cell suspension showed strong alkalization upon illumination in different unbuffered salt solutions, abolished by the addition of the protonophore to the cell suspension (Fig. 1A). Therefore, *Bc*XeR acts as an inward light-driven proton pump. Spectroscopic properties of the *Bc*XeR showed that the maximum absorption wavelength of *Bc*XeR in purified solubilized form is 558 nm and remains stable in a wide range of pH values, similar to that found for other XeRs⁴⁻⁶ (Extended Data Fig. 2A).

The photocycle kinetics of BcXeR was determined using time-resolved visible light absorption spectroscopy (Fig. 1B). The model of the photocycle was validated by investigations of temperature dependences and an Arrhenius plot (Extended Data Fig. 2B). Similar to other XeRs, BcXeR demonstrates a fast formation of the K state, followed by the rise of the early L state in a microsecond (Fig. 1B, Extended Data Fig. 2). Within approx. 20 ms the strongly blue-shifted M state characteristic to the deprotonated RSB is formed^{4–6,9} (Fig. 1B). The formation of the M state coincides in time with the first step of proton transfer within BcXeR, as evidenced by the generation of the membrane electric potential in the lipid vesicles with the rhodopsin in response to a ns green light flash (Extended Data Fig. 2C; Supplementary Note 1). Then, the M state biexponentially decays directly to the ground state with half-times of 70 ms and 0.8 s. The M decay coincides in time with the second notable proton transfer stage identified by a further change of the membrane electric potential inside the proteoliposomes containing BcXeR upon laser illumination (Extended Data Fig. 2C; Supplementary Note 1).

Next, we crystallized BcXeR using *in meso* approach and solved its ground state structure at 1.7 Å resolution¹⁰ (Table 1; see Methods for details). The photocycle of the crystallized protein is similar to that in solution, indicating that the protein remains functional in crystals (Fig. 1C, D; Extended Data Fig. 2C,D). The L state in crystals is at its highest occupancy at 30 µs and persists up to 1 ms (Fig. 1C). The M state is at its maximum occupancy at 20 ms and decays to the ground state in seconds (Fig. 1D). BcXeR forms trimers in crystals similar to those of other trimeric MRs, such as bacteriorhodopsin from Halobacterium salinarum (HsBR) and a XeR from Nanosalina (NsXeR)^{6,11,12} (Extended Data Fig. 3). The protein protomer has seven transmembrane α -helices (A to G) (Fig. 1E; Extended Data Fig. 3). The BC loop at the extracellular part of the protein forms a 9 Å long β -sheet (Extended Data Fig. 3). The cofactor retinal is in its all-trans configuration in the ground state and is covalently bound to K207 of helix G via the protonated RSB (Fig. 1E; Extended Data Fig. 4A).

The cytoplasmic part of *Bc*XeR contains a large cavity between S211 and the pair of carboxylic residues E34 and D214, directly exposed to the cytoplasm (Fig. 1F). The cavity is separated from the RSB by an 8 Å

135 hydrophobic gap and is filled with water molecules mediating an H-bond network between the carbonyl 136 oxygen of K207 to the E34-D214 pair (Fig. 1F). D214 is stabilized by T88. The role of these residues was 137 studied in detail for other bacterial XeRs using functional tests of their mutant forms and also FTIR studies^{4,5}. 138 Our mutational analysis of BcXeR showed consistent results (Extended Data Fig. 5; Supplementary Note 2). 139 Indeed, the data suggest multiple roles of this region in XeRs functioning throughout a single photocycle. 140 First, it works as a proton acceptor from the RSB upon the formation of the M state. This is supported by our 141 analysis of the pH dependence of the M state formation (Extended Data Fig. 2H). We showed that the rise of 142 the M state does not depend on pH in the range between 6 and 9.5 meaning that there should be an internal 143 proton acceptor from the RSB. Moreover, the rise of the M state is delayed at pH lower than 5, where the E34-144 D214 pair becomes protonated according to our structural data (Supplementary Note 3). Consequently, in the 145 M state, the region of the E34-D214 pair is a transient proton storage place. Lastly, it also acts as a proton 146 release group during the M-to-ground state transition. Thus, the region is a transit point for the proton coming 147 from the RSB before its release to the cytoplasm. Therefore, we denote this cluster as a proton transit group 148 (PTG) of BcXeR by an analogy with the proton release group (PRG) of HsBR formed by E194-E204 pair and 149 surrounding polar amino acid residues (Fig. 1F; Extended Data Fig. 6C,D)^{11,13}.

150151

152

153

154

155

156

157

158

The RSB region is critical for proton translocation in *BcXeR* and is conserved within XeRs (Extended Data Fig. 5; Supplementary Note 2). At the extracellular side of *BcXeR*, there is a quasi-continuous H-bond network propagating from the bulk to the RSB of *BcXeR*, which is only disrupted near Y49 (Fig. 1G; Extended Data Fig. 7C). The central residue in this network, R70, is oriented towards a large cavity, which leads to the extracellular bulk and is filled with numerous water molecules (Fig. 1G). According to our mutational analysis, R70 is essential for inward proton pumping, unlike D118, E192, and E195, which surround the cavity (Extended Data Fig. 5; Supplementary Note 2). More details on the structure of *BcXeR* in the ground state is given in Supplementary Note 4.

159

Structures of BcXeR in the L and M intermediate states

161

160

162 To follow the early structural rearrangements in BcXeR associated with the L state formation we used two 163 complementary approaches. First, since the L state is accumulated in the BcXeR crystals in sub-ms time scales 164 (Fig. 1C), we obtained a structural snapshot of the protein with a 500-µs-long X-ray exposure at 2.3 Å 165 resolution with a 250 µs delay to the trigger of a 532-nm laser flash using time-resolved serial crystallography (Fig. 2A; Table 2). Hereafter, we refer to it as a 250-750-us snapshot. Thus, we obtained time-resolved 166 167 structural data on BcXeR at a synchrotron source with a time resolution of 500 µs, which is one order of magnitude higher than that shown in the studies on MRs^{14,15} (Fig. 2B). Second, we determined the structure 168 169 of the cryotrapped L state in a single BcXeR crystal at 1.6 Å resolution (Table 1). For that, the cryocooled 170 crystal was warmed up to 170 K and illuminated for 6 min with a 633-nm laser; then, the crystal was cooled 171 down to 100 K and the X-ray diffraction data were collected (see Methods for details). Similar procedures

172 have already been successfully used for the cryotrapping and structure determination of the L states of HsBR and the light-driven chloride pump halorhodopsin^{16,17}. The microspectrophotometry of the BcXeR crystal 173 174 before and after the procedure indicated the accumulation and trapping of solely the L state (Fig. 2C). The cryotrapping of the L state resulted in almost twice as high occupancy of the intermediate in crystals (35% 175 176 and 20% obtained with cryotrapping and time-resolved crystallography, respectively) as well as a much higher 177 resolution (1.6 Å vs. 2.3 Å). Nevertheless, both structures demonstrate similar structural rearrangements 178 associated with the intermediate state formation, such as the flips of L81, W173, L136 and retinal 179 isomerization (Fig. 2B; Extended Data Fig. 4, 8B,C,F). The R.M.S.D. of the refined coordinates of the L-180 substructures in the cryotrapped and time-resolved data is 0.2 Å. In both cases, the F_o-F_c maps shows no 181 unexplained density above 3.0 σ . However, the structure of the cryotrapped L state demonstrates more essential 182 details such as appearance of key functional water molecules in the region between the RSB and S211 183 (Wat506, Wat507, and Wat508) not observed in the time-resolved L state data (Fig. 2B; Extended Data Fig. 184 4); therefore, hereafter we refer to the cryotrapped L intermediate.

185

186 Next, to visualize the following structural rearrangements accompanying the rise of the M state and a possible 187 subsequent spectrally-silent sub-M state transition during its biexponential decay we first used a time-resolved 188 serial crystallography approach. Namely, we obtained a series of 33 datasets covering in total 250 ms of the 189 BcXeR photocycle with a time resolution of 7.5 ms and a spatial resolution of 2.2 Å (Fig. 2A; Table 2; 190 Extended Data Fig. 8D,E,H,I). Structures of the intermediate states of BcXeR obtained at all 33 time points are identical as also evidenced by their corresponding Folight-Fodark difference electron density maps. 191 192 Nevertheless, we captured the rise of the M state occupancy in the crystals in the range between the 0-7.5 and 193 7.5-15 ms and its gradual decay in the following snapshots (Fig. 2D). Since our time-resolved crystallography 194 data cover a 250 ms time range corresponding to the spectrally-silent past-M state transitions, but do not 195 display any possible associated structural rearrangements, we assume that these past-M state transitions are 196 also structurally-silent (or at least undeterminable at a 2.2 Å resolution).

197

198 Second, following the photocycle data in crystals (Extended Data Fig. 2) clearly indicating that under steady 199 illumination with a 532-nm light the M state is the dominant one, we cryotrapped the M state in a single crystal 200 of BcXeR and solved the structure at 1.7 Å resolution (Table 1). In brief, the crystal was illuminated at 293 K 201 for 1 s with a 532-nm laser beam and cryocooled in nitrogen stream with the light still switched on (see 202 Methods for details). Microspectrophotometry of the BcXeR crystal confirmed the accumulation and trapping 203 of solely the M state (Fig. 2C). Indeed, the cryotrapped structure contained >70% of the M state with atomic 204 structure in perfect agreement with the time-resolved data (the R.M.S.D. of the refined coordinates of the M-205 substructures in the cryotrapped and time-resolved data is 0.2 Å) albeit higher intermediate state occupancy 206 and resolution (Fig. 2B; Extended Data Fig. 4, 8).

Evolution of BcXeR structure in the course of the photocycle

Time-resolved crystallography and cryotrapping of the intermediate states allowed us to follow with high precision the structural rearrangement of BcXeR in the course of inward proton pumping. Since the mechanism of proton pumping by MRs was studied in detail mostly for outward proton pump $HsBR^{13,14,18}$, also serving as a benchmark for studies of many other MRs, we used it as a reference for the analysis of the BcXeR structure and mechanism. We conclude that several aspects of the molecular mechanism of proton translocation in BcXeR differs principally from that of HsBR.

However, it is also based on proton wires, similar to $HsBR^{19}$. We found essential structural rearrangements in the L state of BcXeR resembling those shown for the L state of HsBR. First, similar to HsBR, in BcXeR retinal adopts 13-cis configuration in the L state and the protonated RSB is relocated to the cytoplasmic side (Fig. 2B, Fig. 3A). The π -bulge of the helix G near S206 is enlarged (Fig. 3A; Extended Data Fig. 6E). As clearly seen from the difference electron density maps, the side chain of L81 is distinctly flipped and three water molecules (Wat506, Wat507, and Wat508) emerge between the RSB and S211 (Fig. 3A; Extended Data Fig. 4E). They mediate the linear H-bond chain between the RSB and S211 propagating further to the PTG at the cytoplasmic side (Fig. 3A; Extended Data Fig. 4E). Thus, in the L state, the RSB of BcXeR is stabilized by the linear water-mediated H-bond chain. Notably, the same structural rearrangements and transiently-formed linear H-bond chain were found in the L state of $HsBR^{18-20}$ (Extended Data Fig. 9A). A direct comparison of the L state structures of HsBR and BcXeR demonstrates that, similarly for both proteins, the RSB is H-bonded to the carboxylic residues at the cytoplasmic side of the proteins via a water chain consisting of three water molecules. A similar water chain was found in the N state of HsBR for the reprotonation of the RSB from D96¹⁴.

At the same time, in contrast to HsBR, we found marked rearrangements of the retinal binding pocket of BcXeR, such as the 180°-flip of W173 (analog of W182 in HsBR) (Fig. 2B; Fig. 3B; Supplementary Video 1). In BcXeR this extended conformational change occurs in order to avoid steric conflict with the C20 atom of the isomerized retinal (Fig. 3B). To allow the flip, the L136 side chain is reoriented towards the lipid membrane (Fig. 3B). A water molecule (Wat509) appears near Wat501 to maintain the interaction between helices F and G weakened by the W173 reorientation (Fig. 3B). Wat501 is relocated closer to F210 to provide more space for the reorientation of L81 (Fig. 3B). Also unlike in HsBR, where extended changes in the extracellular part are observed^{16,19}, the corresponding region of BcXeR is preserved in the L state. The PTG also remains unmodified at this stage (Fig. 3A).

In the M state, both time-resolved and cryotrapping data undoubtedly display the retinal in the 13-cis conformation, similar to that in HsBR (Fig. 2B; Extended Data Fig. 4B). The water-mediated H-bond chain connecting the RSB to S211 in the L state disappears in the M state, and the L81 side chain returns back to the ground position (Fig. 3A). Thus, the hydrophobic gate between the RSB and the rest of the cytoplasmic

part is restored, somewhat similar to that found in $HsBR^{18,19}$. The restoration of the gate in BcXeR is essential for preventing proton backflow to the RSB from the cytoplasmic side of the protein.

At the same time, there are unique structural features specific to the M state of *Bc*XeR but not to *Hs*BR. First of all, in *Bc*XeR the RSB is oriented towards helix G and is stabilized by an H-bond to the S206 side chain, while in *Hs*BR the RSB orients toward helix C and is H-bonded to T89 from a DTD signature motif of archaeal outward proton pumps^{18,19} (Fig. 3A; Extended Data Fig. 9B). The H-bond of the RSB to S206 indicates the deprotonated form of the base in the M state, in line with the strong blue-shift of the absorption spectrum of *Bc*XeR at this stage. The helix G is slightly shifted towards the lipid membrane to allow for more space for the 13-*cis* retinal while helix C remains unmodified (Extended Data Fig. 9B). The maximal displacement occurs in the region of P203 (analog of D212 in *Hs*BR), which is a unique characteristic residue in XeRs.

Proton translocation events in BcXeR

The structural data strongly suggests that the PTG becomes protonated in the M state. Indeed, the analysis of the PTG structure in different states of *Bc*XeR showed that there are two principally different conformations of the group (Fig. 3A; Extended Data Fig. 4C,D, 10; Supplementary Note 3). The first is characterized by a sodium ion bound in the PTG coordinated by D214, E34, T88, and carbonyl oxygen of A84. The sodium ion was assigned to the electron density by the analysis of its coordination. In *Bc*XeR, the ion is coordinated by five oxygens with a mean Na-O distance of 2.4 Å, which is expected for this type of ions²¹ (Extended Data Fig. 10). In this sodium-bound conformation, the side chain of E34 is oriented towards D214. This conformation is present in the ground and L states of *Bc*XeR at cryo conditions but could not be found at room temperature (Fig. 3A; Supplementary Note 3). Sodium binding in the PTG reflects the deprotonated state of the group. Thus, the sodium-bound conformation unequivocally corresponds to the deprotonated PTG. Therefore, in the ground and in the L states the PTG is deprotonated, which also agrees well with FTIR data⁴.

In the second conformation of the PTG there is no sodium ion and E34 is reoriented towards the cytoplasm (Fig. 3A; Extended Data Fig. 10). An additional water molecule was found between the E34 and D214 residues. This water molecule is located within 0.8 Å from the position of the sodium ion in the sodium-bound conformation; however, due to the flip of E34 it is only coordinated with four oxygens with a mean O-O distance of 2.8 Å, characteristic to a normal H-bond²². This sodium-free conformation is found in the M state (Fig. 3A). The protonation state of the PTG in the sodium-free conformation is an intriguing and non-trivial question. We determined the structures of the ground state of *BcXeR* in a wide range of pH values (5.2-8.2, Extended Data Fig. 10; Supplementary Note 3). The sodium-free conformation of PTG remains unmodified suggesting that this conformation reflects both deprotonated and protonated forms, which, however, cannot be structurally distinguished, at least at 2 Å resolution (Supplementary Note 3).

Nevertheless, the sodium dissociation from the PTG upon the L-to-M state transition might be a signature of the proton transfer to the group at this stage of the photocycle (Fig. 3A). Since the RSB is deprotonated upon the L-to-M state transition and there is a continuous H-bond chain connecting the RSB to PTG in the L state, we assume that the proton is relocated from the RSB towards the cytoplasm via this linear H-bond chain (Fig. 3A). Thus, the proton released from the RSB is transferred through the proton wire and is likely stored at the PTG in the M state. The direct proton transfer to the cytoplasm from the RSB with the formation of the M state cannot be excluded but is unlikely, according to our time-resolved spectroscopy experiments (Extended Data Fig. 2H).

Next, the extracellular side of *BcX*eR remains almost identical to that in the ground and L states (Fig. 3D). The H-bond network is only slightly modified in the region between H6 and R70 (Fig. 3D; Extended Data Fig. 7C,D). Namely, while one water molecule Wat402 is found in a double conformation in the ground and L states, indicating its weak interaction with Y49 in only half of the protein molecules, two separate water molecules are well-resolved in the M state (Fig. 3D; Extended Data Fig. 7C-E). This minor rearrangement provides a stronger connection between Y49 and Wat402 in the M state, resulting in an almost continuous H-bond chain from the RSB to the large water-filled concavity exposed to the extracellular bulk (Fig. 3D). We suggest that this H-bond chain serves as a pathway, a proton wire, for the RSB reprotonation. It should be noted that although the retinal is in a 13-cis conformation in the M state, the RSB is located already very close to its position in the ground state and is within an H-bond distance from Wat401 (Fig. 3D). Thus, the RSB is accessible for reprotonation from the extracellular bulk. However, spectroscopic data shows that the reprotonation of the RSB proceeds slowly in *BcXeR* and in a pH-independent manner (Fig. 1B; Extended Data Fig. 2H). Therefore, we suggest that the proton translocation from the extracellular side to the RSB requires the formation of a continuous proton wire, which, in turn, is the time-limiting step of the inward proton transport process.

Gating of inward proton translocation in BcXeR

Notably, in the M state of BcXeR the W173 side chain is largely flipped to avoid steric conflict with the 13-cis retinal and is oriented nearly perpendicular to its initial position (Fig. 2B; Fig. 3C; Supplementary Movie 1). L169 is flipped towards helix G to allow the rearrangement of W173. The conformation of W173 in the M state of BcXeR is stabilized by its water-mediated H-bonding to D107 (Fig. 3C). In contrast, W182 in HsBR (analog of W173 of BcXeR) preserves its orientation throughout the photocycle^{14,18,19} (Extended Data Fig. 9C). We suggest that, in BcXeR, W173 can be rotated since there is sufficient place near the T143 residue for this large-scale movement. The reorientation of W173 is also provided by the flip of L169. In HsBR, T143 is substituted by a larger residue L152, which would cause a steric conflict with W182 in the rotated orientation. Moreover, there is a T178 residue at the position of L169 stabilized by an H-bond to a water molecule¹⁹. Thus, we may speculate that in *Hs*BR the flip of W182 is blocked by the presence of the L152 and T178 residues. However, further investigations are needed to probe this hypothesis. The pedal-like pushing of the retinal on the W182 in *Hs*BR is claimed to trigger a 9 Å tilting of the cytoplasmic parts of E and F helices resulting in the opening of the protein for proton uptake through its cytoplasmic part to the RSB¹⁴ (Extended Data Fig. 9C). In contrast, an unusual flexibility of the retinal binding pocket of *Bc*XeR and particularly that of W173 allows mitigation of the large-scale structural rearrangements caused by retinal isomerization resulting in almost no movements of the transmembrane helices (Extended Data Fig. 9C). This helps to maintain the hydrophobic gate at the cytoplasmic part of *Bc*XeR in the closed state after proton translocation from the RSB to the PTG, preventing the backflow of the protons during the M-to-ground state transition. Thus, we suggest that the notable rearrangements of W173 and its surroundings are one of the key determinants of the unidirectional proton transport in bacterial XeRs. Indeed, D107, stabilizing the conformation of W173 in the M state, is shown to be essential for proton pumping in *Bc*XeR (Extended Data Fig. 5; Supplementary Note 2). Moreover, D107 is conserved within bacterial XeRs, but is substituted by glutamine in ASR-like sensors which lack proton-pumping activity²³. Importantly, this is a noteworthy difference between the internal organization of bacterial XeRs and ASR-like sensors (Extended Data Fig. 5).

Finally, our time-resolved crystallography data show that the M-to-ground transition proceeds directly without structurally distinguishable intermediate states. This suggests that the following events occur simultaneously: the retinal returns to the all-*trans* configuration; the RSB is reprotonated from the extracellular side; the W173 and its surroundings are relocated back to the ground conformations; and the PTG releases the proton to the cytoplasm and re-binds the sodium ion. In contrast to *Hs*BR, no large-scale structural rearrangements accompany these events, which is also supported by the absence of the late N- and O-like states in XeRs (Extended Data Fig. 2).

Conclusion

341342

343

344

345

346

347348

349

350

351

352353

354

355

356

357

358

359

360

361

362363

In this work we used bacterial xenorhodopsin BcXeR to study the molecular mechanism of light-driven inward proton translocation (Fig. 4; Supplementary Note 5; Supplementary Video 2). We utilized synchrotron radiation to capture high-resolution snapshots of the early sub-ms and the subsequent ms-time-scale reactions in BcXeR using time-resolved serial crystallography. Thus, this work extends the time range of X-ray synchrotron time-resolved crystallography on microbial rhodopsins to hundreds of microseconds, which is by an order of magnitude shorter than reported earlier¹⁴. Our work is a basis for further time-resolved studies of light-sensitive proteins at synchrotrons and X-ray Free-Electron Lasers. Such further structural information on BcXeR in the ps-ns time range would be beneficial for the deeper understanding of its primary photoreactions. Together with the recent data on the outward proton pump HsBR¹⁹, the present work demonstrates that proton wires are at the core of both outwardly and inwardly directed proton transfer through the membrane serving as pathways within the proteins. In BcXeR, only a minor reorganization of the proton wires accompanied by subsequential opening of two internal gates in the course of the protein function is sufficient for inwardly directed proton translocation. Our results suggest that mutations at the extracellular gate of BcXeR could accelerate the protein photocycle, as is required for the engineering of a potent IPP-based optogenetic tools⁶. Mutational, bioinformatical, and structural analysis of XeRs suggests that the proton wire mechanism is fundamental and characteristic not only for bacterial, but also for archaeal rhodopsins (Supplementary Note 6). We also speculate that proton wires could be universal for other proton transporters. At the same time, we demonstrate that BcXeR differs from outward proton pumps and has a specific cavity-gate-cavity-gate-water pore structure resembling that of channelrhodopsin-2 (ChR2)²⁴. However, in contrast to channelrhodopsins, where all gates are opened simultaneously, in XeRs the gates open sequentially, resulting in unidirectional

364365

proton translocation.

Acknowledgements

366

367 We acknowledge the Structural Biology Group of the European Synchrotron Radiation Facility (ESRF) and 368 the European Molecular Biology Laboratory (EMBL) unit in Hamburg at Deutsche Elektronen-Synchrotron 369 (DESY) for granting access to the synchrotron beamlines. Structural and spectroscopic data obtained at the ESRF have been recorded and analyzed between 2020 and 2021. This work was supported by the common 370 371 program of Agence Nationale de la Recherche (ANR), France and Deutsche Forschungsgemeinschaft, 372 Germany (ANR-15-CE11-0029-02), and by funding from Frankfurt: Cluster of Excellence Frankfurt 373 Macromolecular Complexes (to E.B.) by the Max Planck Society (to E.B.) and by the Commissariat à 374 l'Energie Atomique et aux Energies Alternatives (Institut de Biologie Structurale)-Helmholtz-Gemeinschaft 375 Deutscher Forschungszentren (Forschungszentrum Jülich) Special Terms and Conditions 5.1 specific 376 agreement. V.G. greatly acknowledge his HGF professorship. This work used the icOS and HTX platforms 377 of the Grenoble Instruct-ERIC center (ISBG; UAR 3518 CNRS-CEA-UJF-EMBL) within the Grenoble 378 Partnership for Structural Biology (PSB). Platform access was supported by FRISBI (ANR-10-INBS-0005-379 02) and GRAL, a project of the University Grenoble Alpes graduate school (Ecoles Universitaires de 380 Recherche) CBH-EUR-GS (ANR-17-EURE-0003). Protein expression and spectroscopic analysis were 381 supported by the Russian Science Foundation (RSF) (project 21-64-00018). This work was supported by the 382 project ANR-19-CE11-0026. K.K. has been supported by EMBL Interdisciplinary Postdoctoral Fellowship 383 (EIPOD4) under Marie Sklodowska-Curie Actions Cofund (grant agreement number 847543). The work of 384 A.A. was supported by funding of the German Research Foundation to Dr. Tobias Moser via the Multiscale 385 Bioimaging - Cluster of Excellence (EXC 2067/1-390729940). Time-resolved crystallography data treatment 386 was supported by RFBR (project 19-29-12022). A.K. acknowledges the support from the Ministry of Science 387 and Higher Education of the Russian Federation (agreement 075-03-2023-106, project FSMG-2021-0002). 388 A.Rog. acknowledges the Ministry of Science and Higher Education of the Russian Federation (project no. 389 075-01645-22-06/720000F.99.1.B385AV67000). X-ray data collection was supported by the Russian 390 Ministry of Science and Higher Education (grant no. 075-15-2021-1354). The research of electrogenic 391 behavior of BcXeR in proteoliposomes was carried out at the expense of the grant of the Russian Science 392 Foundation No. 22-14-00104 (to S.S.).

393394

Author Contributions Statement:

395 K.K., A.A., and F.T. contributed equally and either has the right to list himself first in bibliographic 396 documents. A.A. found a gene bioinformatically, proposed it as a target and performed initial functional tests 397 in E. coli; F.T. did cloning, expression, and purification of the protein and its mutants; F.T. did functional 398 studies of the proteins in E.coli cell suspension; A.A. supervised the expression and purification; S.S. 399 performed studies of electrogenic behavior of BcXeR in proteoliposomes; D.S. and F.T. performed flash-400 photolysis studies on protein in solution and in crystals; I.C. supervised flash-photolysis experiments; K.K. 401 crystallized the protein; R.A. helped with the crystallization; S.B., R.A., and A.Roy. performed cryotrapping 402 of the intermediates at the icOS Lab and recorded the spectra of the states in crystals; K.K. performed

cryotrapping of the intermediates in crystals at the P14 beamline; M.A. installed the laser setup at the P14 404 beamline for the cryotrapping and TR studies; K.K. collected and processed the diffraction data, solved and refined the structures; G.B. helped with data collection, structure refinement, and analysis; M.N. provided 406 online monitoring of X-ray diffraction images during TR crystallography data collection at 1 kHz; D.v.S. provided scripts for serial data processing and help with serial data analysis; V.S., N.I., E.B., T.R.S., A.Rog., 408 F.R.-V., V.B., and G.B. helped with data analysis; A.K. animated the transitions between the intermediates under the supervision of I.G.; A.A. performed bioinformatic analysis with the help of R.R.; F.T., A.A., K.K., 409 410 and V.G. analyzed the results and prepared the manuscript with the important contribution of G.B. and with input from all the other authors. V.G. supervised and analyzed the results of experiments and proposed the 412 conception of molecular mechanism of inward proton transport.

413 414

411

403

405

407

Competing Interest Statement:

415 Authors declare no competing interests.

Table 1. Data collection and refinement statistics on BcXeR at 100 K.

	Ground state, pH 8.2	L state, pH 8.2	M state, pH 8.2	Ground state, pH 7.0	M state, pH 7.0	Ground state, pH 5.2	M state, pH 5.2	Ground state, pH 7.6, no	M state, pH 7.6, no Na
	0.2			7.0		3.2		7.6, no Na	no na
PDB ID	7ZMY	7ZN3	7ZN0	7ZN8	7ZN9	7ZNA	7ZNB	7ZNC	7ZND
Data collection									
Space group	P 21 21 21	P 21 21 21	P 21 21 21	P 21 21 21	P 21 21 21	P 21 21 21	P 21 21 21	P 21 21 21	P 21 21 21
Cell									
dimensions									
a, b, c (Å)	68.24,	68.39,	68.50,	68.60,	68.90,	68.57,	68.50,	68.45,	69.09,
, ,	109.57,	109.49,	109.50,	109.60,	109.50,	109.59,	109.50,	109.63,	109.36,
	119.47	119.39	119.00	119.30	119.40	119.62	119.00	118.46	119.31
α, β, γ (°)	90, 90,	90, 90,	90, 90,	90, 90,	90, 90,	90, 90,	90, 90,	90, 90,	90, 90,
.,.,	90	90	90	90	90	90	90	90	90
Resolution	49.799-	49.763-	49.738-	49.798-	49.767-	49.817-	49.738-	44.790-	59.792-
(Å)	1.700	1.600	1.700	2.200	2.300	1.800	1.900	1.700	1.985
	(1.742-	(1.739-	(1.813-	(2.293-	(2.370-	(1.916-	(1.963-	(1.780-	(2.168-
	1.700)*	1.600)*	1.700)*	2.200)*	2.300)*	1.800)*	1.900)*	1.700)*	1.985)*
R_{merge} , %	7.9	7.6	8.3	16.3	17.7	10.4	7.8	9.5	11.4
	(335.3)	(283.5)	(346.9)	(377.5)	(246.4)	(337.6)	(194.8)	(280.8)	(163.6)
$I/\sigma I$	15.9 (0.9)	15.9 (1.1)	16.5 (0.8)	10.9(0.8)	9.6 (1.3)	14.1 (0.8)	17.5 (1.5)	15.0 (0.9)	13.7 (1.3)
Completeness	92.0	92.3	93.9	85.5	96.3	94.5	95.3	96.2	90.2
(%)	(65.4)	(75.8)	(82.4)	(66.6)	(78.3)	(88.6)	(79.6)	(86.3)	(77.0)
Redundancy	13.8	13.7	13.0	13.1	13.2	13.1	13.1	13.3	12.0 (7.2)
	(14.1)	(13.0)	(13.1)	(12.0)	(12.8)	(13.1)	(12.2)	(12.5)	
Refinement	20.1.7	20.1.6	20.17	20.2.2	20.22	20.1.0	20.1.0	20.1.7	20.1.00
Resolution (Å)	20-1.7	20-1.6	20-1.7	20-2.2	20-2.3	20-1.8	20-1.9	20-1.7	20-1.98
No.	86,518	78,514	65,890	35,350	36,269	62,007	59,830	78,775	40,266
reflections	00,510	70,514	05,070	33,330	30,207	02,007	37,030	70,773	40,200
$R_{\text{work}} / R_{\text{free}}$	17.4/20.3	20.4/21.6	19.9/22.7	19.9/23.8	21.6/25.3	19.6/23.0	19.6/22.7	18.5/20.8	25.0/28.2
Occupancy of	-	35	100	-	100	17.0/25.0	100	-	100
the		33	100		100		100		100
intermediate,									
%									
No. atoms									
Protein	5301	5490	5351	5301	5342	5304	5342	5362	5236
Retinal	60	120	60	60	60	60	60	60	60
Sodium	3	3	-	3	_	3	_	_	_
Lipid	737	599	627	732	626	720	627	807	802
Water	283	246	241	281	243	289	240	375	75
B-factors									
Protein	33	30	34	36	38	31	34	27	32
Retinal	27	28	29	27	32	25	29	20	26
Sodium	26	25	-	36	-	25	-	-	-
Lipid	60	47	58	58	60	58	58	54	60
Water	46	39	44	48	45	45	44	42	33
R.m.s.									
deviations									
Bond	0.006	0.014	0.002	0.004	0.002	0.004	0.002	0.003	0.002
lengths (Å)									
Bond	1.223	1.649	1.019	1.091	1.019	1.131	1.022	1.078	0.994
angles (°)									

^{*}Values in parentheses are for highest-resolution shell.

Table 2. Serial crystallography data collection and refinement statistics on BcXeR at room temperature.

Table 2. Serial crystallography data collection and refinement statistics on BcXeR at room temperature.								
	Dark state, pH 8.2	7.5-15.0 ms snapshot,	Dark state, pH 8.2	250-750 μs snapshot, pH				
	7.5 ms exposure	pH 8.2	500 μs exposure	8.2				
PDB ID	7ZNE	7ZNI	7ZNG	7ZNH				
Data collection								
Space group	P 21 21 21	P 21 21 21	P 21 21 21	P 21 21 21				
Cell								
dimensions								
a, b, c (Å)	71.50, 111.50, 119.30	71.50, 111.50, 119.30	71.91, 111.86, 119.52	71.91, 111.86, 119.52				
α, β, γ (°)	90, 90, 90	90, 90, 90	90, 90, 90	90, 90, 90				
Indexed patterns	67,912	12,449	17,997	17,526				
Indexing rate, %	33.9	10.4	25.0	24.3				
Resolution (Å)	45.8-2.1 (2.17-2.10)*	45.8-2.2 (2.28-2.20)*	45.96-2.30 (2.38-2.30)*	45.96-2.30 (2.38-2.30)*				
$R_{\rm split}$, %	6.6 (156.74)	14.3 (198.8)	19.2 (260.1)	19.6 (292.3)				
$I/\sigma I$	9.0 (0.6)	4.5 (0.5)	4.0 (0.4)	3.9 (0.4)				
Completeness	100.0 (100.0)	100.0 (100.0)	100.0 (100.0)	100.0 (100.0)				
(%)	•		•	, ,				
Redundancy	926.8 (629.9)	177.3 (121.1)	526.2 (360.9)	507.4 (348.2)				
CC*, %	99.9 (72.0)	99.4 (42.2)	99.6 (42.5)	99.6 (41.4)				
Refinement								
Resolution (Å)	20-2.1	20-2.2	20-2.3	20-2.3				
No. reflections	54,544	47,347	41,079	40,880				
$R_{ m work}$ / $R_{ m free}$	18.7/21.5	18.5/21.4	21.8/25.1	22.0/24.8				
Occupancy of	-	62	-	20				
the intermediate,								
%								
No. atoms								
Protein	5189	5507	5194	5383				
Retinal	60	120	60	120				
Lipid	528	566	540	540				
Water	75	95	75	75				
B-factors								
Protein	55	56	48	49				
Retinal	46	50	38	36				
Lipid	63	65	66	67				
Water	62	63	55	54				
R.m.s.								
deviations								
Bond lengths	0.002	0.010	0.002	0.006				
(Å)								
Bond angles	1.050	1.428	1.040	1.250				
(°)								

^{*}Values in parentheses are for highest-resolution shell.

426 Figure Legends

Figure 1 | Functional, spectroscopical, and structural features of BcXeR. A. Light-induced pH changes in suspension of E.coli expressing BcXeR in non-buffered salt solutions (salt molarity is 100 mM each). Solid lines represent experiments in the absence of any protonophore, dashed lines show pH changes in the presence of 30 μ M of protonophore carbonyl-cyanide m-chlorophenyl-hydrazone (CCCP). The yellow area indicates the period of time when the light was on. B. Photocycle scheme of BcXeR. C. Time-resolved traces of BcXeR in solution and in crystals at 480 nm characteristic for the L state. D. Time-resolved traces of BcXeR in solution and in crystals at 390 nm characteristic for the M state. E. Overall side view of the BcXeR protomer. F. Detailed view of the cytoplasmic side of BcXeR in the ground state. The proton transit group (PTG) is highlighted in yellow. The hydrophobic gate between the RSB and S211 is shown with a red arrow. G. Detailed view of the extracellular side of BcXeR. The gate near Y49 is shown with a red arrow. Cavities were calculated using HOLLOW²⁵ and are shown with a blue surface. Hydrogen bonds are shown with black dashed lines.

Figure 2 | Obtaining of BcXeR structures in the L and M intermediate states. A. A global fit of flash-photolysis data revealed the presence of three spectrally distinct states of BcXeR: K, L, and M. Time regions captured in two time-resolved (TR) experiments are highlighted in red and in yellow for the L and M states, respectively. B. Examples of F_o^{light} - F_o^{dark} difference electron density maps in the region of retinal obtained with TR and cryotrapping methods. The maps are contoured at the level of 3.5σ. The maps of the L state obtained with TR approach are contoured at 3.0σ. In the latter case the maps appear weaker due to a lower resolution and a lower occupancy of the intermediate. C. UV-visible absorption spectra measured in crystallo at 100 K of the ground (green solid), the L (red solid), and M (yellow solid) states (insets in the right panel: photos of the same frozen BcXeR crystal in the cryoloop before and after the laser illumination, near the corresponding spectra). Spectra of the corresponding states of the BcXeR photocycle in solution are shown with dashed lines. D. Evolution of the occupancy of the M state determined from the TR crystallography experiments (red bars). Red bars indicate the experimental error of the M state occupancy determination (±2%). The evolution is in line with the difference absorption evolution at 390 nm (yellow line) corresponding to the M state population determined by TR spectroscopy of the BcXeR crystals.

Figure 3 | **Structural rearrangements in** *Bc***XeR in the L and M states. A.** Structural rearrangements at the cytoplasmic part of *Bc*XeR in the course of the photocycle. Blue arrows indicate the key conformational changes. The wide light blue arrow indicates the putative pathway for proton translocation. Three water molecules appearing in the L state and forming a transient H-bond chain from the RSB to S211 are highlighted in yellow. The proton at the PTG in the M state is highlighted in light blue. The key hydrogen atoms are shown as white spheres. **B.** Structural rearrangements in the retinal and retinal binding pocket upon the ground-to-L transition. Black arrows indicate the most notable conformational changes between the ground (green) and the L (salmon) states. **C.** Structural rearrangements in the retinal and retinal binding pocket upon the L-to-M transition. Black arrows indicate the most notable conformational changes between the L (salmon) and the M (yellow) states. H-bonds connecting D107 and W173 via water molecule Wat501' are shown with yellow dashed lines. **D.** Extracellular side of *Bc*XeR in the ground (green), L (salmon), and M (yellow) states. The continuous H-bond connecting the RSB to the concavity (highlighted with light blue surface) exposed to the extracellular bulk is shown with yellow dashed lines. The blue arrow indicates the additional water molecule Wat403 found only in the M state. The wide light blue arrow indicates the putative pathway for RSB reprotonation.

Figure 4 | **Proposed mechanism of inward proton transport by BcXeR.** The putative scheme of the key structural rearrangements during the **BcXeR** photocycle is shown. Inactive regions of the proton wire propagating through the inside of the protein are shown with yellow thick dashed lines. Active regions of the wire are shown with green thick dashed lines. Positively and negatively charged groups are colored blue and red, respectively. The protein surface is shown in light gray. Water molecules involved in the proton wire are shown as red spheres. Sodium ions are shown as purple spheres. The retinal cofactor is colored cyan. Central hydrophobic and weak extracellular gates are marked and indicated with arrows. The states of the gates are indicated with the color of the arrow and a corresponding description (red - closed; green - opened; yellow - intermediate). Blue arrows indicate putative proton translocation pathways. The lipid membrane is shown in blue.

- 481 References
- 482 1. Gushchin, I. & Gordeliy, V. Microbial Rhodopsins. in Membrane Protein Complexes: Structure and
- 483 Function (eds. Harris, J. R. & Boekema, E. J.) 19–56 (Springer, 2018). doi:10.1007/978-981-10-7757-
- 484 9 2.
- 2. Oesterhelt, D. & Stoeckenius, W. Rhodopsin-like Protein from the Purple Membrane of Halobacterium
- 486 halobium. *Nature*. *New Biol*. **233**, 149–152 (1971).
- 487 3. Sahel, J.-A. et al. Partial recovery of visual function in a blind patient after optogenetic therapy. Nat.
- 488 *Med.* **27**, 1223–1229 (2021).
- 489 4. Inoue, K. et al. A natural light-driven inward proton pump. Nat. Commun. 7, 13415 (2016).
- 490 5. Inoue, S. et al. Spectroscopic characteristics of Rubricoccus marinus xenorhodopsin (RmXeR) and a
- 491 putative model for its inward H+ transport mechanism. *Phys. Chem. Chem. Phys.* **20**, 3172–3183 (2018).
- 492 6. Shevchenko, V. et al. Inward H + pump xenorhodopsin: Mechanism and alternative optogenetic
- 493 approach. *Sci. Adv.* **3**, e1603187 (2017).
- 494 7. Weissbecker, J. et al. The Voltage Dependent Sidedness of the Reprotonation of the Retinal Schiff Base
- Determines the Unique Inward Pumping of Xenorhodopsin. Angew. Chem. Int. Ed. 60, 23010–23017
- 496 (2021).
- 497 8. Alcaraz, L. D. et al. The genome of Bacillus coahuilensis reveals adaptations essential for survival in the
- relic of an ancient marine environment. *Proc. Natl. Acad. Sci. U. S. A.* **105**, 5803–5808 (2008).
- 499 9. Chizhov, I. et al. Spectrally silent transitions in the bacteriorhodopsin photocycle. Biophys. J. 71, 2329–
- 500 2345 (1996).
- 501 10. Landau, E. M. & Rosenbusch, J. P. Lipidic cubic phases: A novel concept for the crystallization
- of membrane proteins. *Proc. Natl. Acad. Sci.* **93**, 14532–14535 (1996).
- 503 11. Luecke, H., Schobert, B., Richter, H.-T., Cartailler, J.-P. & Lanyi, J. K. Structure of bacteriorhodopsin at
- 504 1.55 Å resolution. *J. Mol. Biol.* **291**, 899–911 (1999).
- 505 12. Hasegawa, N., Jonotsuka, H., Miki, K. & Takeda, K. X-ray structure analysis of bacteriorhodopsin at
- 506 1.3 Å resolution. *Sci. Rep.* **8**, 13123 (2018).
- 507 13. Gerwert, K., Freier, E. & Wolf, S. The role of protein-bound water molecules in microbial rhodopsins.
- 508 Biochim. Biophys. Acta BBA Bioenerg. **1837**, 606–613 (2014).

- 509 14. Weinert, T. et al. Proton uptake mechanism in bacteriorhodopsin captured by serial synchrotron
- 510 crystallography. *Science* **365**, 61–65 (2019).
- 511 15. Mous, S. et al. Dynamics and mechanism of a light-driven chloride pump. Science 375, 845–851 (2022).
- 512 16. Wickstrand, C., Dods, R., Royant, A. & Neutze, R. Bacteriorhodopsin: Would the real structural
- intermediates please stand up? *Biochim. Biophys. Acta BBA Gen. Subj.* **1850**, 536–553 (2015).
- 17. Kouyama, T., Kawaguchi, H., Nakanishi, T., Kubo, H. & Murakami, M. Crystal Structures of the L1,
- 515 L2, N, and O States of pharaonis Halorhodopsin. *Biophys. J.* **108**, 2680–2690 (2015).
- 18. Nango, E. et al. A three-dimensional movie of structural changes in bacteriorhodopsin. Science 354,
- 517 1552–1557 (2016).
- 518 19. V. Borshchevskiy et al. True-atomic-resolution insights into the structure and functional role of linear
- chains and low-barrier hydrogen bonds in proteins. *Nat. Struct. Mol. Biol.* (2022) doi:10.1038/s41594-
- 520 022-00762-2.
- 521 20. Freier, E., Wolf, S. & Gerwert, K. Proton transfer via a transient linear water-molecule chain in a
- membrane protein. *Proc. Natl. Acad. Sci.* **108**, 11435–11439 (2011).
- 523 21. Kuppuraj, G., Dudev, M. & Lim, C. Factors Governing Metal-Ligand Distances and Coordination
- Geometries of Metal Complexes. *J. Phys. Chem. B* **113**, 2952–2960 (2009).
- 525 22. Szalewicz, K. Hydrogen Bond. in Encyclopedia of Physical Science and Technology (Third Edition) (ed.
- Meyers, R. A.) 505–538 (Academic Press, 2003). doi:10.1016/B0-12-227410-5/00322-7.
- 527 23. Jung, K.-H., Trivedi, V. D. & Spudich, J. L. Demonstration of a sensory rhodopsin in eubacteria. *Mol.*
- 528 *Microbiol.* **47**, 1513–1522 (2003).
- 529 24. Volkov, O. et al. Structural insights into ion conduction by channelrhodopsin 2. Science 358, eaan8862
- 530 (2017).

- 531 25. Ho, B. K. & Gruswitz, F. HOLLOW: Generating Accurate Representations of Channel and Interior
- Surfaces in Molecular Structures. *BMC Struct. Biol.* **8**, 49 (2008).

535 Methods

536

537

Phylogenetic analysis of rhodopsin genes

- To retrieve xenorhodopsins from available sequence data, a two-step procedure based on sequence similarity search and Hidden Markov Models was followed. First, bona fide XeR amino acid sequences were queried against the non-redundant database at NCBI using Diamond v0.9.4.105²⁶ and applying the substitution matrix BLOSUM45 to retrieve distantly related proteins with the E-value set to 1e-5. Next, all genomes whose proteins gave hits with bona fide XeR were downloaded and all encoding rhodopsins (either XeR-related or other types) were identified using HMMER version v3.3.2 (http://hmmer.org) and further confirmed by checking for the presence of 7 transmembrane domains using TMHMM²⁷.
- The obtained set of putative xenorhodopsins was aligned with ClustalO. The phylogenetic tree was constructed in iTol v.6²⁸. Structurally important regions were identified manually according to the obtained high-resolution structure of *BcXeR*, taking into account structure-functional information on *NsXeR*, ASR, and other published xenorhodopsins. The data and figures, showing conserved amino acids in the structurally important regions, were calculated and designed in an in-house Python Jupyter notebook and Wolfram Mathematica.

551

552

Cloning

BcXeR coding DNA was optimized for *E.coli* codons using GeneArt (Thermo Fisher Scientific). Genes were synthesized commercially (Eurofins). For protein expression and measurements of pump activity pET15b plasmid with 6xHis-tag at the C-terminal was used. Site-directed mutagenesis with PCR, phosphorylation and ligation was performed.

557

558

Protein expression, solubilization, and purification

559 E.coli cells were transformed with pET15b plasmid containing the gene of interest. Transformed cells were 560 grown at 37°C in shaking baffled flasks in an autoinducing medium ZYP-5052²⁹, containing 10 mg/L 561 ampicillin. They were induced at an OD₆₀₀ of 0.6-0.7 with 1 mM isopropyl-β-D-thiogalactopyranoside 562 (IPTG). Subsequently, 10 µM all-trans-retinal was added. Incubation continued for 3 hours. The cells were 563 collected by centrifugation at 5000g for 20 min. Collected cells were disrupted in an M-110P Lab 564 Homogenizer (Microfluidics) at 25,000 p.s.i. in a buffer containing 20 mM Tris-HCl, pH 7.5, 5% glycerol, 565 0.5% Triton X-100 (Sigma-Aldrich) and 50 mg/L DNase I (Sigma-Aldrich). The membrane fraction of the 566 cell lysate was isolated by ultracentrifugation at 125,000g for 1 h at 4°C. The pellet was resuspended in a 567 buffer containing 50 mM NaH₂PO₄/Na₂HPO₄, pH 7.5, 0.15 M NaCl and 1% DDM (Anatrace, Affymetrix) 568 and stirred overnight for solubilization. The insoluble fraction was removed by ultracentrifugation at 125,000g 569 for 1h at 4 °C. The supernatant was loaded on an Ni-NTA column (Qiagen), and protein was eluted in a buffer containing 50 mM NaH₂PO₄/Na₂HPO₄, pH 7.5, 0.15 M NaCl, 0.4 M imidazole and 0.05% DDM. The eluate 570 571 was subjected to size-exclusion chromatography on a 125-ml Superdex 200 PG column (GE Healthcare Life

Sciences) in a buffer containing 50 mM NaH₂PO₄/Na₂HPO₄, pH 7.5, 0.15 M NaCl and 0.05% DDM. In the end protein was concentrated to 70 mg/ml for crystallization and -80°C storage.

574

575

576

577578

579

580

581

582

583

Measurements of pump activity in the E. coli cells suspension

The proteins (*Bc*XeR, *Aa*SR, *Ppa*SR) were expressed as described above. The cells were collected by centrifugation at 4000g for 15 min and were washed three times with an unbuffered salt solution, with 30-min intervals between the washes to allow for exchange of the ions inside the cells with the bulk. After that, the cells were resuspended in an unbuffered salt solution and adjusted to an OD₆₀₀ of 8.5. The measurements were performed in 3-ml aliquots of stirred cell suspension kept at ice temperature (0.3-1.0°C). The cells were illuminated using a halogen lamp (Olympus KL2500 LCD), and the light-induced pH changes were monitored with a pH meter (SevenEasy, METTLER TOLEDO). The measurements were repeated under the same conditions after the addition of 30 μM CCCP protonophore.

584585

Spectroscopic characterization and time-resolved absorption spectroscopy

- 586 The absorption spectra in pH range were obtained with Biotek Synergy HT. The setup for time-resolved 587 absorption spectroscopy was as follows. A brilliant B Nd:YAG laser (Quantel, France) was used for providing 588 pulses of 4 ns duration at a 532 nm wavelength and an energy of about 2 mJ/pulse. Samples were placed 589 between two collimated mechanically coupled monochromators (LSH-150, LOT, Germany). The probing 590 light (Xe-arc lamp, 75 W, Hamamatsu, Japan) passed the first monochromator and the sample and arrived 591 after a second monochromator at a PMT detector (R12829, Hamamatzu, Japan). Two digital oscilloscopes 592 (Keysight DSO-X 4022A) were used to record the traces of transient transmission changes in two overlapping 593 time windows.
- In this setup we recorded transient absorption changes starting from 700 ns after the laser pulse until the completion of the photocycle, at each wavelength from 330 to 730 nm in 10-nm steps, 25 laser pulses were averaged to improve the signal-to-noise ratio. We analyzed the data sets using the global multiexponential nonlinear least-squares fitting program MEXFIT as reported earlier.

598

599

Electrometric Time-Resolved Measurements of the Membrane Potential

600 The generation of the transmembrane electric potential difference $\Delta \Psi$ was observed using a direct 601 electrometric setup with a time resolution of 100 ns as described earlier. ^{30,31}. Proteoliposomes with protein 602 were fused with the surface of a collodion phospholipid-impregnated film (a measuring membrane) separating 603 two sections of the measuring cell filled with a buffer solution. The potential difference $\Delta\Psi$ across the 604 measuring membrane were detected by Ag+/AgCl electrodes immersed in the solution at both sides of 605 membrane. This membrane should be thin enough and possess large electric capacitance (about 5 nF) for 606 detecting fast charge translocation events. Typical resistance of the measuring membrane was 2 to 3 GOhm. 607 A Nd-YAG laser (YG-481, $\lambda = 532$ nm, pulse half-width 12 ns, pulse energy up to 40 mJ; Quantel) was used as a light source of the light pulses. In the process of the light-driven proton transfer, rhodopsin creates $\Delta\Psi$ across the vesicle membrane, which is proportionately divided by the measuring membrane.

611 **Proteoliposomes preparation**

608

609

610

612

613

614

615

616

617

618

619

620

636

Protein containing proteoliposomes were prepared as described previousely³². Soybean asolectin was dissolved (1% w/v in final solution) in chloroform, which was then removed using a rotary evaporator (25°C) and a vacuum pump. Asolectin film was resuspended in 0.1 M NaCl, 2% (w/v) sodium cholate to the final asolectin concentration of 1% (w/v). Suspension was sonicated for 5 min at 4°C and centrifuged. Supernatant was sonicated for 1 min and then solubilized protein was quickly added to the final concentration 0.7 mg/ml which was followed by adding detergent-absorbing beads (Amberlite XAD-2, Sigma-Aldrich). The beads were exchanged with new ones several times (one of them was kept overnight and the others were close to an hour each).

621 Crystallization

- The crystals of BcXeR were grown with an *in meso* approach¹⁰, similar to that used in our previous works^{33,34}.
- 623 In particular, the solubilized protein (60 mg/ml) in the crystallization buffer was mixed with premelted at 42°C
- monoolein (MO, Nu-Chek Prep) in a 3:2 ratio (lipid:protein) to form a lipidic mesophase. The mesophase was
- homogenized in coupled syringes (Hamilton) by transferring the mesophase from one syringe to another until
- a homogeneous and gel-like material was formed.
- For the growing of single crystals of BcXeR used for determination of the cryo structures, 150 nl drops of a
- 628 protein-mesophase mixture were spotted on a 96-well LCP glass sandwich plate (Marienfeld) and overlaid
- with 400 nL of precipitant solution by means of the NT8 crystallization robot (Formulatrix). The best crystals
- were obtained with a protein concentration of 20 mg/ml (in the water part of the mesophase). The crystals for
- the determination of the BcXeR structures in the ground and M states at pH 5.2, 7.0, and 8.2 and in the L state
- at pH 8.2 were obtained using 0.8 M Na/K-Pi pH 8.2 as a precipitant. The crystals for the determination of
- 633 the BcXeR structures in the ground and M state at pH 7.6 in the absence of sodium were obtained using 1.2
- M (NH₄)₃PO₄ pH 7.6 as a precipitant. The crystals were grown at 22°C and appeared in 2 months. Once the
- 635 crystals reached their final size, crystallization wells were opened, and drops containing the protein-

mesophase mixture were covered with 100 µl of the respective precipitant solution. For the data collection,

- harvested crystals were incubated for 5 min in the respective precipitant solutions. For obtaining the structures
- of *Bc*XeR at pH 5.2 the crystallization well was covered with a solution of 1.2 M Na/K-Pi pH 5.2. The crystals
- 639 were soaked for 24 hours with exchanging the buffer three times. Crystals were then harvested using
- micromounts (Mitegen, USA), flash-cooled and stored in liquid nitrogen.
- For time-resolved serial crystallography, crystals of BcXeR were grown in 200-µl PCR tubes. For that, 0.8-
- 642 1.6 μl of precipitant solution (3.2 M Na/K-Pi pH 8.2) were dispensed at the bottom of the PCR tube and
- 643 covered with 12 µl of the mesophase from the Hamilton syringe. The PCR tube was quickly closed and
- centrifuged for 1 min at 6000g at 22°C to sediment the phase to the bottom of the PCR tube. The PCR tubes

were kept at 22°C. The crystals of BcXeR appeared within 1 week and reached $30x20x5 \mu m^3$ in size. The crystals from several PCR tubes were collected into a single PCR tube using centrifugation for 2 min at 20,800g and 22°C. Then, the bottom part of the PCR tube with the mesophase was cut and inserted upside down into the sealed 200 µl pipette tip. The tip was sealed at the very end using the gas burner. The tip with the inserted PCR tube part was then centrifuged at 6000g and 22°C for 2 minutes using a 1.5 ml tube as an adaptor for the centrifuge rotor. After the centrifugation, the mesophase was found in the sealed tip. The empty PCR tube part was removed and the tip was covered from the wide end with Parafilm to avoid dehydration of the crystals. The plunger was removed from an empty clean 100 µl Hamilton syringe and the syringe was sealed from the side of the needle using Parafilm. The tip with mesophase was cut from the narrow end and inserted into the back side of the prepared Hamilton syringe. The syringe with the inserted tip were fixed in the 50 ml falcon tube; for that, the syringe was wrapped into the paper towel to fit tightly into the falcon tube. Then, the tube with the syringe were centrifuged at 6000g and 22°C for 3 minutes to transfer the mesophase from the tip into the syringe. After the centrifugation, the tip was removed, the syringe was coupled to another clean 100 ul Hamilton syringe and the plunger was slowly inserted into the first syringe. Thus, the phase was slowly transferred into the second syringe. In the case of excessive precipitant solution and/or air, the system was uncoupled for their removal and then coupled back to homogenize the mesophase with crystals. The mesophase was homogenized before the experiment using an LCP-coupler.

Accumulation of the intermediate state in BcXeR crystals

Absorption spectra of *BcX*eR in solution were collected using a UV-2401PC spectrometer (Shimadzu, Japan). The spectroscopic characterization of the L and M states in *BcX*eR crystals was performed at the *icOS* Lab located at the ESRF³⁵. Briefly, UV-visible absorption spectra were measured using as a reference light that of a DH-2000-BAL deuterium-halogen lamp (Ocean Optics, Dunedin, FL) connected to the incoming objective via a 200 µm diameter fiber, resulting in a 50 µm focal spot on the sample, and a QE65 Pro spectrometer (Ocean Optics, Dunedin, FL) connected to the outgoing objective via a 400 µm diameter fiber. The actinic light comes from 532-nm or 633-nm lasers (CNI Laser, Changchun, P.R. China) coupled to a 1000 µm diameter fiber which is connected to the third objective whose optical axis is perpendicular to those of the ingoing and outgoing objectives. All spectra (100 ms acquisition time averaged 20 times) were collected on crystals flash-cooled in liquid nitrogen and kept under a cold nitrogen stream at 100 K.

For the accumulation and cryotrapping of the L state, a crystal was warmed to 170 K and put under constant 633-nm-laser illumination for 6 min at 170 K. During the illumination the crystal was rotated 3 times by 90 degrees to illuminate it from all sides (1.5 minutes for each side). Then the laser was switched off and the crystal was cooled back to 100 K. For the accumulation of the L state the laser power density was 32 W/cm² at the position of the sample. A UV-visible absorption spectrum was subsequently recorded to show the slightly blue-shifted absorption maximum characteristic of the L state of *BcXeR*. The laser power was adjusted to maximize the fraction of the accumulated L state; the absence of destructive effect of the laser on crystals

was justified by the remaining diffraction quality after the cryotrapping procedure as well as by the full return of the protein to the ground state after short test annealing of the crystal to 293 K after cryotrapping of the L state.

685 For the accumulation and cryotrapping of the M state, the crystal was originally kept at 100 K. It was then 686 illuminated by a 532-nm-laser with the nitrogen stream simultaneously blocked for 2 seconds. Due to the short illumination time the crystal was not rotated during the illumination. For better illumination, the crystal was 687 688 oriented with the largest plane perpendicular to the laser beam. The laser was then switched off once the 689 crystal was back at 100 K. For the accumulation of the M state a laser power density of 10 W/cm² at the 690 position of the sample was used. A UV-visible absorption spectrum was subsequently recorded to show the 691 strongly blue-shifted absorption maximum characteristic of the M state of BcXeR. The laser power was 692 adjusted to maximize the fraction of the accumulated M state; the absence of destructive effect of the laser on 693 crystals was justified by the remaining diffraction quality after the cryotrapping procedure as well as by the 694 full return of the protein to the ground state after short test annealing of the crystal to 293 K after cryotrapping of the M state. 695

The mean size of the crystals was $200x100x20 \mu m^3$. The plate-like crystals were oriented so that the largest plane $(200x100 \mu m^2)$ was perpendicular to the laser beam. The laser beam was focused to the size of $200x200 \mu m^2 (1/e^2)$.

A similar setup for the accumulation and cryotrapping of the intermediate states in the *Bc*XeR crystals was established at the P14 beamline of the PETRAIII synchrotron source (Hamburg, Germany) for X-ray diffraction data collection. Also, the same accumulation procedure was applied to crystals at *ic*OS and P14 beamline. In the case of the M state the trapping of the strongly blue-shifted M intermediate state characteristic for the deprotonated RSB was directly visible by a notable change of the crystal color in the micro loop before/after the cryotrapping procedure.

705

706

Single-crystal diffraction data collection and treatment

707 Single-crystal X-ray diffraction data of all structures except the one of the ground state of BcXeR obtained at 708 pH 7.6 in the absence of sodium were collected at the P14 beamline of PETRAIII (Hamburg, Germany) using 709 an EIGER X 16M and EIGER2 X 16M CdTe detectors. The data of the ground state of BcXeR at pH 7.6 in 710 the absence of sodium were collected at the ID23-1 beamline of the ESRF (Grenoble, France) using a 711 PILATUS 6M-F detector. The data collection was performed using MxCube2 software. Diffraction images were processed using XDS³⁶. The reflection intensities were scaled and merged using the Staraniso server³⁷. 712 713 There is no possibility of twinning for the crystals. In all cases, diffraction data from a single crystal were 714 used. The data statistics are presented in Table 1.

Structure determination and refinement of the ground state of BcXeR

Initial phases for the ground state of trimeric BcXeR at pH 8.2 with sodium were successfully obtained in the P2₁2₁2₁ space group by molecular replacement using MOLREP³⁸ from the CCP4 program suite³⁹ using the 1XIO structure of *Anabaena* sensory rhodopsin⁴⁰ as a search model. The initial models were iteratively refined using REFMAC5⁴¹ and Coot⁴². The phases for all other structures of BcXeR determined in the course of the study were determined using MOLREP with the phases of the ground state of BcXeR at pH 8.2 in the presence of sodium.

723

724

716

Structure refinement of the cryotrapped L and M intermediates of BcXeR

725 For the determination of the L state structure of BcXeR two datasets were collected using the same crystal. 726 First, data were collected from a part of the not-yet illuminated crystal. These data correspond to the ground state of BcXeR (we refer to the structure factors corresponding to this dataset as F_0^{dark}). Then, the L state was 727 728 cryotrapped in the same crystal using the above-described protocol. Then, the second dataset was collected 729 from a laser illuminated but not yet X-ray exposed region of the crystal. These data correspond to the intermediate state (we refer to the structure factors corresponding to this dataset as F_olight). Although the F_o-F_c 730 and F₀ light-F₀ dark difference electron density maps clearly indicated structural rearrangements associated with 731 732 the intermediate state formation, the fraction of the L state was not sufficient for direct fitting of the model 733 into $2F_0$ - F_c electron density maps corresponding to the second dataset. Therefore, to build the initial model of 734 the L state we used extrapolated structure factors, calculated from two isomorphous datasets using linear approximation as follows: $F_0^{\text{extrapolated}} = (1/\alpha)^* (F_0^{\text{light}} - (1-\alpha)^* F_0^{\text{dark}})$, where α is the occupancy of the L state. 735 736 The α value was screened while calculating the extrapolated maps from 0.1 to 0.5 with a step of 0.05, and was 737 selected to be 0.3 via an analysis of the electron density maps built using extrapolated structure factors. Then the model of the L state was built manually in Coot using 2Foextrapolated-Fc electron density maps in accordance 738 with the F_olight-F_odark difference electron density maps. The positions of residues 81, 136, 173, 205-210 of the 739 740 protein molecule and several internal water molecules were refined manually compared to the ground state as 741 identified by the strongest peaks at the F_olight-F_odark difference electron density maps. Then, the new positions 742 of the above-mentioned residues and water molecules were added to the ground state model as a second 743 conformation (named conformation C in the final model of the L state). The combined model was 744 automatically refined against the original data using PHENIX. Only atom positions of the L state were refined; 745 the atom positions of the ground state were fixed. B-factor were also refined for all atoms. Analysis of the 746 resulting model and electron density maps showed consistency of the L state structure with the crystallographic data and the F_olight-F_odark difference electron density maps. The final occupancy of the L state 747 748 after refinement was 35%.

In the case of the M state at pH 8.2 in the presence of sodium, the occupancy of the intermediate was high as also evidenced by the color of the crystals after the cryotrapping procedure (the crystal was almost completely

751 yellow, corresponding to the M state of BcXeR). Therefore, the structure of the M state was directly built 752 using 2F_o-F_c electron density maps. After several iterations of manual refinement in Coot and automated 753 refinement using REFMAC5, some peaks at the F_o-F_c difference electron density maps corresponding to a 754 small amount of the L state appeared near residues W173, L136, and S206 (Extended Data Fig. 7B); therefore, 755 these residues were fitted with double conformation in the final model of the M state, where conformations A 756 and B correspond to the M and L states, respectively. In the case of the M states at other pH values and sodium 757 concentrations the structure of the intermediate was refined iteratively in Coot and REFMAC5 using the model 758 of the M state at pH 8.2 in the presence of sodium as a starting model (Supplementary Table 1).

759

760

777

778

779

780

781

782

783

784

785

Serial crystallography data collection and treatment

761 Serial crystallography data of BcXeR was obtained at RT at the P14 beamline of PETRA III (Hamburg, 762 Germany) using an EIGER2 X 16M CdTe detector and a 2 (vertical) x 7 (horizontal) µm² sized beam at 12.7 keV (2x10¹² and 2x10¹³ ph/s in the cases of experiments with 500 μs and 7.5 ms X-ray exposures, 763 764 respectively). The data collection was performed using MxCube2 software. In the case of the time-resolved 765 crystallography experiments with 7.5 ms X-ray exposures the X-ray beam was attenuated to 10% to reduce 766 the X-ray dose. The crystals were delivered into the X-ray beam in a stream of mesophase provided by high-767 viscosity LCP injector⁴³. The mesophase containing protein crystals was loaded into the 20-μl-reservoir of the 768 LCP injector without additives directly from the Hamilton syringe. The injector was oriented at 20° from 769 vertical. The extrusion of the mesophase containing the BcXeR crystals was performed using capillaries with 770 50 and 100 µm diameters for the collection of the 250-750-µs snapshot and the series of 7.5-ms-long 771 snapshots, respectively. The mesophase stream was stabilized by a helium gas stream. A 50 µm capillary was 772 used in the case of the fast data collection to reduce sample consumption. The linear speed of the injected 773 mesophase was estimated using high-speed camera recordings and was 2.5 and 0.5 mm/s, respectively. The 774 serial crystallography data collection and treatment statistics are given in Table 2. The overall scheme of data 775 collection was similar to that used in earlier time-resolved crystallography studies of HsBR at a synchrotron 776 source¹⁴.

Two sets of serial crystallography data of the dark state of *Bc*XeR were collected as a reference for the time-resolved studies. First, the data of the dark state were collected using a 500-µs-long X-ray data acquisition per image at a frame rate of 1 kHz using the central 4M region of the EIGER2 X 16M CdTe detector. A total number of 72,000 detector images were collected and processed with CrystFEL⁴⁴ (version 0.9.1) without any additional modification. Potential crystal hits were identified with SNR=4, --threshold=7, --highres=2.3 using the peakfinder8 algorithm as implemented in CrystFEL. The second dataset of the dark state was collected using 7.5-ms-long X-ray diffraction data acquisition per image at a frame rate of 133 Hz using the 16M region of the EIGER2 X 16M CdTe detector. A total number of 199,980 detector images were collected and processed with CrystFEL (version 0.9.1) without any additional modification. Potential crystal hits were

786 identified with SNR=5, --threshold=20, --highres=2.1 using peakfinder8 algorithm as implemented in 787 CrystFEL. In both cases, the initial geometry, provided by the beamline data staff, was optimized with 788 detector-shift. Cell unit parameters were iteratively adjusted from the initial parameters taken from single-789 crystal cryo data. For indexing, indexer XGANDALF⁴⁵ was used with the --multi option enabled. Integration 790 was performed using --int-radius=3,4,5. This yielded datasets with 17,997 and 67,912 indexed images, 791 yielding 21,569 and 80,082 crystals for the datasets with 500-μs-long and 7.5-ms-long X-ray data acquisition 792 per frame, respectively. Data were merged using partialator with -model=unity, --symmetry=mmm, and 793 number of iterations=1. Finally, 21,533 and 79,892 crystals were used for merging together after partialator 794 rejection.

Time-resolved crystallography data on the L state of BcXeR (250-750-µs snapshot) were collected by illuminating the crystals at a 40 Hz repetition rate with a 532 nm pump laser focused to the laser spot directly at the intersection between the crystal stream and the X-ray beam of 60 μ m in diameter (1/e²). Per each laser pulse a series of 25 consecutive snapshots was collected. The length of the laser pulse was 500 µs. The energy of a single laser pulse was 6.2 µJ with laser power density of 438 W/cm², which is ~11 times higher than the power density used in previous time-resolved studies of microbial rhodopsins at a synchrotron source^{14,15}. Nevertheless, due to the short laser pulse these illumination conditions resulted in an uncorrected value of ~15-65 photons per retinal depending on crystal orientation (protein concentration in crystals was 21 mM and an extinction coefficient value used was 50,000 M⁻¹cm⁻¹); however, this calculation does not account for the laser beam scattering by the jet and light absorption by the mesophase itself. The latter issue is especially valid in the case of BcXeR, since the final mesophase in which the crystals were delivered was not fully transparent probably due to the change of the phase type under crystallization conditions. We assume that the abovementioned factors reduce the real number of photons per retinal molecule. Nevertheless, the experiment was performed in a multiphoton regime. The laser power was set to its maximum value in order to increase the occupancy of the intermediate state. Analysis of the diffraction patterns collected with and without laser illumination showed that the diffraction quality was not affected by the laser illumination. Data were collected at a frame rate of 1 kHz using the central 4M region of the EIGER2 X 16M CdTe detector. The start of the Xray diffraction data acquisition for each series was electronically delayed by 250 µs relative to the optical laser trigger. The overall time of data collection from a sample with a total volume of 20 µl was about 40 minutes.

813814

795

796

797

798

799

800

801

802

803

804

805

806

807

808

809

810

811

812

815 A total number of 72,000 detector images were collected for the 250-750-µs snapshot and processed with 816 CrystFEL (version 0.9.1) without any additional modification. Potential crystal hits were identified with SNR=4, --threshold=7, --highres=2.3 using the peakfinder8 algorithm as implemented in CrystFEL. For 817 indexing, indexer XGANDALF⁴⁵ was used with the --multi option enabled. Integration was performed using 818 819 --int-radius=3,4,5. This yielded a dataset with 17,527 indexed images and 20,908 crystals. This means that approx. 19% of the images contained multiple diffraction patterns. Data were merged using partialator with -820 821 model=unity, --symmetry=mmm, and number of iterations=1. Finally, 20,866 crystals were used for merging 822 together after partialator rejection.

Time-resolved crystallography data of the M state of BcXeR (7.5-ms-long snapshot) were collected by illuminating the crystals at a 4 Hz repetition rate with a 532 nm pump laser focused to the laser spot directly at the intersection between the crystal stream and the X-ray beam of 180 µm in diameter (1/e²). Per each laser pulse a series of 33 consecutive snapshots was collected. The laser was triggered simultaneously with the detector. The length of the laser pulse was 7.5 ms. The energy of a single laser pulse was 540 µJ with laser power density of 283 W/cm², which is ~7.5 times higher than the power density used in previous time-resolved studies of microbial rhodopsins at a synchrotron source^{14,15}. These illumination conditions resulted in an uncorrected value of ~150-600 photons per retinal depending on crystal orientation (protein concentration in crystals was 21 mM and an extinction coefficient value used was 50,000 M⁻¹cm⁻¹); however, this calculation does not account for the laser beam scattering by the jet and light absorption by the mesophase itself. The latter issue is especially valid in the case of BcXeR, since the final mesophase in which the crystals were delivered was not fully transparent probably due to the change of the phase type under crystallization conditions. We assume that the above-mentioned factors reduce the real number of photons per retinal molecule. Nevertheless, the experiment was performed in a multiphoton regime. The laser power was set to its maximum value in order to increase the occupancy of the intermediate state. Analysis of the diffraction patterns collected with and without laser illumination showed that the diffraction quality was not affected by the laser illumination. Data were collected at a frame rate of 133 Hz using the 16M region of the EIGER2 X 16M CdTe detector. Use of the 16M detector vs its 4M mode (as in the 500 µs time-resolved experiment) allows for a large sample-detector distance and a reduced background. The higher resolution of the 7.5 ms data vs the 500 µs data at lower dose is due to the use of the 16M mode. Since 7.5 ms is the shortest exposure period of EIGER2 X CdTe detector in a standard 16M mode, the 7.5 ms time resolution was chosen to sample the time interval of 0 to 250 ms. Moreover, the size of the laser spot, the laser pulse duration, the repetition rate of laser pulses, the jet speed and X-ray flux were set to match this time interval. Increasing the frame rate would require a proportional increase in the jet speed and hence in the sample consumption (by an order of magnitude), and a decrease in the duration of the laser pulse leading to lower M state occupancy. The start of the X-ray diffraction data acquisition for each series was electronically synchronized to the optical laser trigger. The overall time of data collection from a sample with a total volume of 40 µl was about 5 hours.

849850

823

824

825

826

827

828

829830

831832

833

834

835

836

837

838

839

840841

842

843

844

845

846

847

848

851 A total number of 3,958,702 detector images were collected and processed with CrystFEL (version 0.9.1) 852 without any additional modification. Among the collected images, potential crystal hits were identified with 853 SNR=5, --threshold=20, --highres=2.2 using the peakfinder8 algorithm as implemented in CrystFEL, corresponding to an average hit rate of 10.8%. For indexing, indexer XGANDALF⁴⁵ was used with the --multi 854 855 option enabled. Integration was performed using --int-radius=3,4,5. This yielded a dataset with 389,438 856 indexed images and 428,729 crystals. Data were scaled and merged together using partialator with -857 model=unity, --symmetry=mmm, and number of iterations=1 and datasets for each time point were splitted by partialator using the --custom-split option. Finally, 427,677 crystals were used for merging and splitting 858 859 after partialator rejection. 12,449 crystals were merged for the 7.5-15-ms snapshot.

860861

Time-resolved serial crystallography structure refinement

862

867

868

869

870

871

872

873

874

875

876877

878

879880

881

882883

884

885 886

887 888

889

890

891

892

893

894

895

The models of the ground state of *Bc*XeR at room temperature determined via serial crystallography were built iteratively using the structure of *Bc*XeR at 100 K as a starting model using Coot and REFMAC5. The structures of the ground state of *Bc*XeR at room temperature in the cases of the 500-µs-long and the 7.5-ms-long X-ray data acquisition per frame were identical (Extended Data Fig. 8).

In the case of the 250-750-µs snapshot the Fo^{light}-Fo^{dark} difference electron density maps built in PHENIX⁴⁶ identified structural rearrangement at the residues 81, 173, 136, and 207 similar to those shown in the case of the cryotrapped L intermediate. However, in the case of time-resolved data, the occupancy of the intermediate, the resolution, and the overall quality of the data were lower. Therefore, the model of the L state obtained with the cryotrapping procedure was used as a starting model for the automated refinement in REFMAC5. The additional water molecules appearing in the L state but not seen in the time-resolved data were removed from the starting model. Only atom positions of the L state were refined; the atom positions of the ground state were fixed. B-factor were also refined for all atoms. The final occupancy of the L state in the case of time-resolved serial crystallography data was 20%.

In the case of the series of 33 7.5-ms-long snapshots of the BcXeR following the laser excitation, the F_olight-F₀^{dark} difference electron density maps built in PHENIX for each time point were similar and identified structural rearrangements almost identical to those shown in the case of the cryotrapped M intermediate at all 33 time points. F_o^{dark} corresponds to the dark state of BcXeR, F_o^{light} corresponds to each of the 33 datasets collected following the laser excitation in the time-resolved experiments. To build the model of the intermediate state we used extrapolated structure factors, calculated from two isomorphous datasets using linear approximation as follows: $F_0^{\text{extrapolated}} = (1/\alpha)^* (F_0^{\text{light}} - (1-\alpha)^* F_0^{\text{dark}})$, where α is the occupancy of the intermediate state. For each time point, the α value was screened while calculating the extrapolated maps from 0.1 to 0.5 with a step of 0.05, and was selected to be in the range of 0.4-0.5, time-point dependent, via an analysis of the electron density maps built using extrapolated structure factors. Subsequently, the model of the intermediate state was manually built in Coot using electron density maps calculated using extrapolated structure factors in accordance with the Folight-Fodark difference electron density maps. The manual building was performed for the 7.5-15-ms snapshot since it has the highest α value (0.5) corresponding to the highest occupancy of the intermediate state. After that, the combined model was prepared containing the structures of the ground and the intermediate states as alternative conformations (A and C, respectively). Then, the model was automatically refined in REFMAC5 against each of the 33 datasets. Only atom positions of the M state were refined; the atom positions of the ground state were fixed. B-factor were also refined for all atoms. The analysis of the resulting intermediate state structures and electron difference maps confirmed their identity to that of the M state of BcXeR obtained at 100 K. Final occupancies were identified using occupancy refinement performed in REFMAC5. It showed that the occupancy of the M state varies from 62% (at the 7.5-15-ms

snapshot) to 43% (at the 240-247.5-ms snapshot). For the occupancy refinement all atom positions and B-factors were fixed. Since all the models were identical and only differ in the occupancy of the intermediate state, here we have only reported the one with the highest occupancy of the state (7.5-15-ms snapshot) (Table 2).

Analysis of the X-ray radiation damage of the BcXeR crystallography data

The X-ray-induced radiation damage is a critical issue in studying of microbial rhodopsins as demonstrated earlier for $HsBR^{47}$. The most prominent signs of the X-ray radiation damage appear as negative difference densities at the HsBR D85 (analog of D76 in BcXeR) and water molecules in close proximity of the RSB. The decarboxylation rates were determined⁴⁷ at 12-15% MGy⁻¹.

In order to assess possible influence of X-ray-induced radiation damage on the findings presented in this work, we estimated the X-ray dose for each of the reported datasets. In all cases, the X-ray dose rates were calculated using RADDOSE (v4.0.1020)⁴⁸. The parameters used for calculation and the resulting doses are given in Supplementary Table 2. In our single-crystal data average doses did not exceed 1.1 MGy, which corresponds to less than 17% expected decarboxylation. Consistently, we have not observed any negative electron densities at carboxylic residues including D76, as well as at water molecules near the RSB and in other regions.

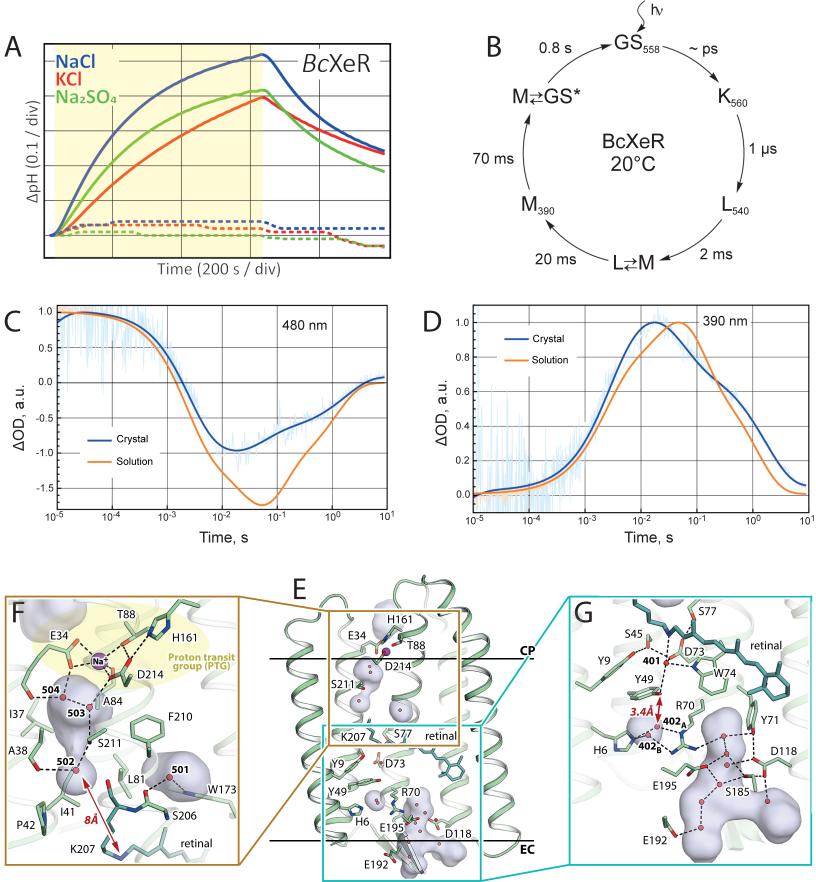
In the case of time-resolved experiments the data were collected in the shutterless mode, therefore the total exposure time was estimated as the time within which the jet front traverses the full beam width at half maximum, accounting for the 20° angle of the jet to vertical (1 and 5 ms for the fast and slow time-resolved experiments, respectively). In case of the fast experiment, the traversal time is longer than the detector integration time. Therefore, the average exposure to the beam effectively contributing to diffraction data varies uniformly between 0.5 ms (at any point entering the beam during detector frame integration) and 1.0 ms (at any point exiting the beam). Resulting average exposure time 0.75 ms was used for estimating the average dose (400 kGy). We have not observed any signs of X-ray-induced radiation damage in the electron densities of the serial time-resolved crystallography data. Thus, also a minor fraction of the molecules was damaged by X-rays the effects of this does were not visible at 2.2-2.3 Å resolution.

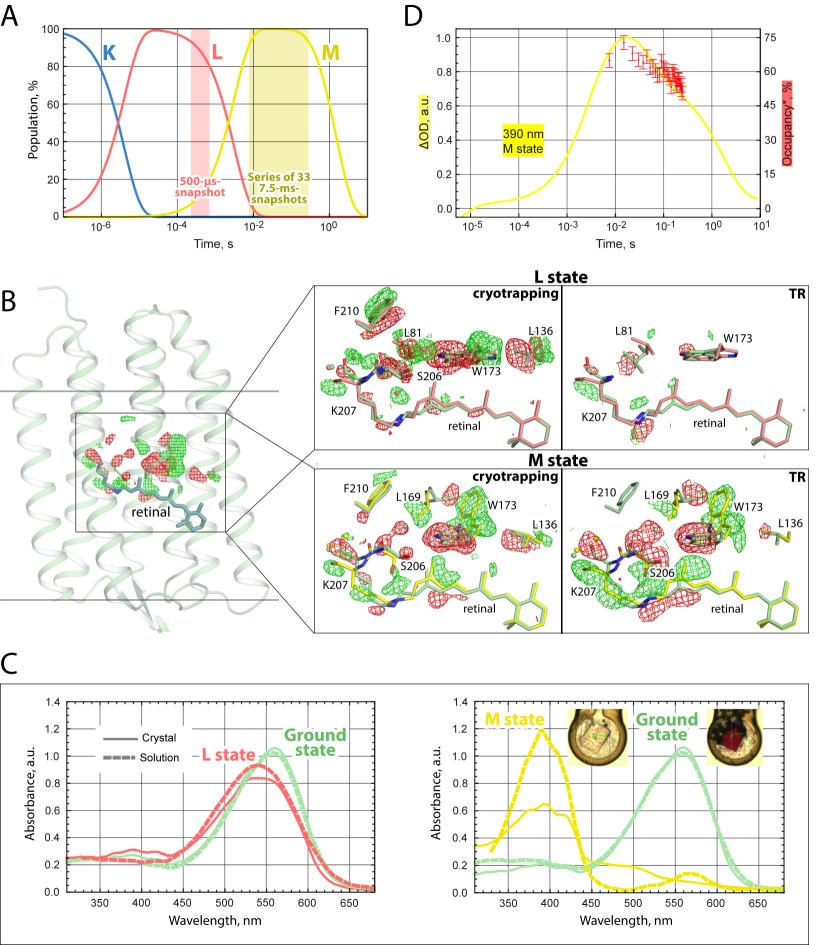
Data Availability

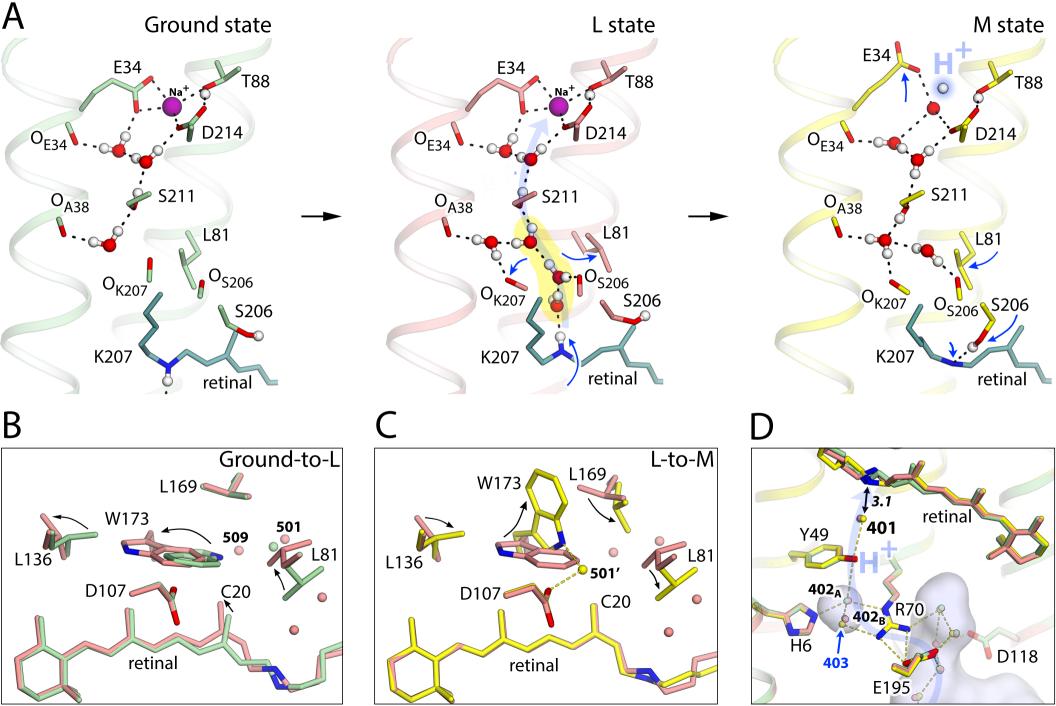
Atomic models built using X-ray crystallography data have been deposited in the RCSB Protein Data Bank with PDB codes 7ZMY (for the ground state at pH 8.2 at 100 K), 7ZN3 (for the L state at pH 8.2 at 100 K), 7ZN0 (for the M state at pH 8.2 at 100 K), 7ZN8 (for the ground state at pH 7.0 at 100 K), 7ZN9 (for the M state at pH 7.0 at 100 K), 7ZNA (for the ground state at pH 5.2 at 100 K), 7ZNB (for the M state at pH 5.2 at 100 K), 7ZNC (for the ground state at pH 7.6 at 100 K in the absence of sodium), 7ZND (for the M state at pH 7.6 at 100 K in the absence of sodium), 7ZND (for the M state at pH 7.6 at 100 K in the absence of sodium), 7ZNE (for the ground state at pH 8.2 at 293 K with 7.5-ms-long exposure), 7ZNI (for the 7.5-15-ms snapshot at pH 8.2 at 293 K), 7ZNG (for the ground state at pH 8.2 at 293 K with 500-μs-long exposure), and 7ZNH (for the 250-750-μs snapshot at pH 8.2 at 293 K). Extrapolated structure factors and phases for the intermediate states of *BcXeR* are available from Zenodo (10.5281/zenodo.7612803). Publicly available in RCSB Protein Data Bank structures of *NsXeR* (PDB ID: 6EYU) and *Hs*BR (PDB IDs: 5ZIL, 7Z0D, 7Z0E, 6RPH) were used for analysis.

- 937 Methods-only References
- 938 26. Buchfink, B., Xie, C. & Huson, D. H. Fast and sensitive protein alignment using DIAMOND. *Nat.*
- 939 *Methods* **12**, 59–60 (2015).
- 940 27. Krogh, A., Larsson, B., von Heijne, G. & Sonnhammer, E. L. Predicting transmembrane protein
- topology with a hidden Markov model: application to complete genomes. J. Mol. Biol. 305, 567–580
- 942 (2001).
- 943 28. Letunic, I. & Bork, P. Interactive Tree Of Life (iTOL) v5: an online tool for phylogenetic tree display
- and annotation. *Nucleic Acids Res.* **49**, W293–W296 (2021).
- 945 29. Studier, F. W. Protein production by auto-induction in high-density shaking cultures. *Protein Expr.*
- 946 *Purif.* **41**, 207–234 (2005).
- 30. Drachev, L. A. et al. Direct measurement of electric current generation by cytochrome oxidase, H+-
- 948 ATPase and bacteriorhodopsin. *Nature* **249**, 321–324 (1974).
- 949 31. Drachev, L. A., Kaulen, A. D., Khitrina, L. V. & Skulachev, V. P. Fast Stages of Photoelectric Processes
- 950 in Biological Membranes. Eur. J. Biochem. 117, 461–470 (1981).
- 951 32. Rokitskaya, T. I. et al. Rhodopsin Channel Activity Can Be Evaluated by Measuring the Photocurrent
- Voltage Dependence in Planar Bilayer Lipid Membranes. *Biochem. Mosc.* **86**, 409–419 (2021).
- 953 33. Kovalev, K. et al. Molecular mechanism of light-driven sodium pumping. Nat. Commun. 11, 2137
- 954 (2020).
- 955 34. Bratanov, D. et al. Unique structure and function of viral rhodopsins. Nat. Commun. 10, 4939 (2019).
- 956 35. von Stetten, D. et al. In crystallo optical spectroscopy (icOS) as a complementary tool on the
- 957 macromolecular crystallography beamlines of the ESRF. Acta Crystallogr. D Biol. Crystallogr. 71, 15–
- 958 26 (2015).
- 959 36. Kabsch, W. XDS. Acta Crystallogr. D Biol. Crystallogr. 66, 125–132 (2010).
- 960 37. STARANISO (http://staraniso.globalphasing.org/cgi-bin/staraniso.cgi).
- https://staraniso.globalphasing.org/staraniso FAO.html.
- 962 38. Vagin, A. & Teplyakov, A. MOLREP: an Automated Program for Molecular Replacement. J. Appl.
- 963 *Crystallogr.* **30**, 1022–1025 (1997).

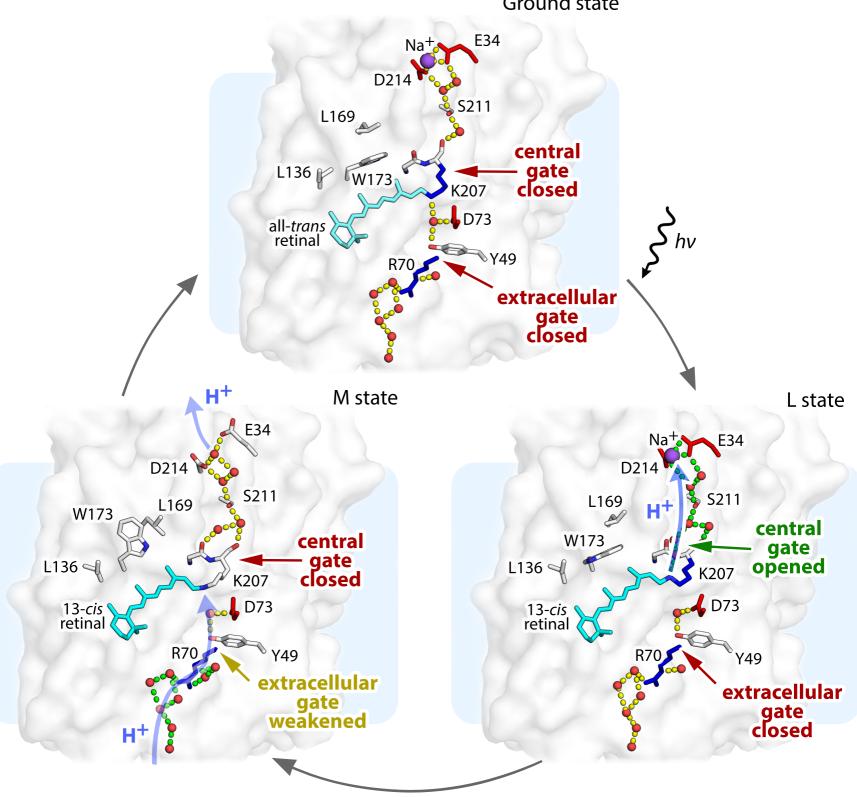
- 964 39. Winn, M. D. et al. Overview of the CCP4 suite and current developments. Acta Crystallogr. D Biol.
- 965 *Crystallogr.* **67**, 235–242 (2011).
- 40. Vogeley, L. et al. Anabaena Sensory Rhodopsin: A Photochromic Color Sensor at 2.0 Å. Science **306**,
- 967 1390–1393 (2004).
- 968 41. Murshudov, G. N. et al. REFMAC5 for the refinement of macromolecular crystal structures. Acta
- 969 *Crystallogr. D Biol. Crystallogr.* **67**, 355–367 (2011).
- 970 42. Emsley, P., Lohkamp, B., Scott, W. G. & Cowtan, K. Features and development of Coot. *Acta*
- 971 *Crystallogr. D Biol. Crystallogr.* **66**, 486–501 (2010).
- 972 43. Weierstall, U. et al. Lipidic cubic phase injector facilitates membrane protein serial femtosecond
- 973 crystallography. *Nat. Commun.* **5**, 3309 (2014).
- 974 44. White, T. A. et al. CrystFEL: a software suite for snapshot serial crystallography. J. Appl. Crystallogr.
- 975 **45**, 335–341 (2012).
- 976 45. Gevorkov, Y. et al. XGANDALF extended gradient descent algorithm for lattice finding. Acta
- 977 *Crystallogr. Sect. Found. Adv.* **75**, 694–704 (2019).
- 978 46. Adams, P. D. et al. PHENIX: a comprehensive Python-based system for macromolecular structure
- 979 solution. Acta Crystallogr. D Biol. Crystallogr. 66, 213–221 (2010).
- 980 47. Borshchevskiy, V. I., Round, E. S., Popov, A. N., Büldt, G. & Gordeliy, V. I. X-ray-Radiation-Induced
- Changes in Bacteriorhodopsin Structure. J. Mol. Biol. 409, 813–825 (2011).
- 982 48. Paithankar, K. S. & Garman, E. F. Know your dose: RADDOSE. Acta Crystallogr. D Biol. Crystallogr.
- 983 **66**, 381–388 (2010).

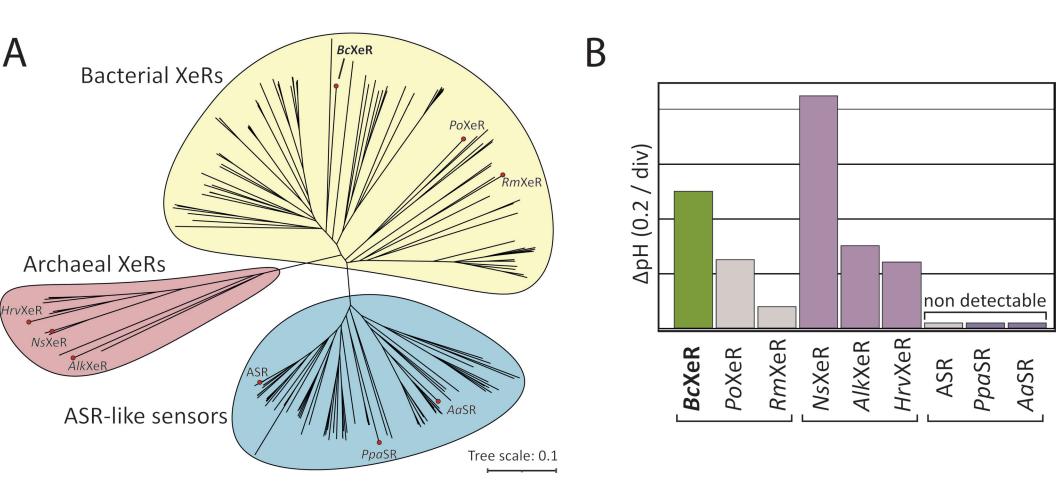


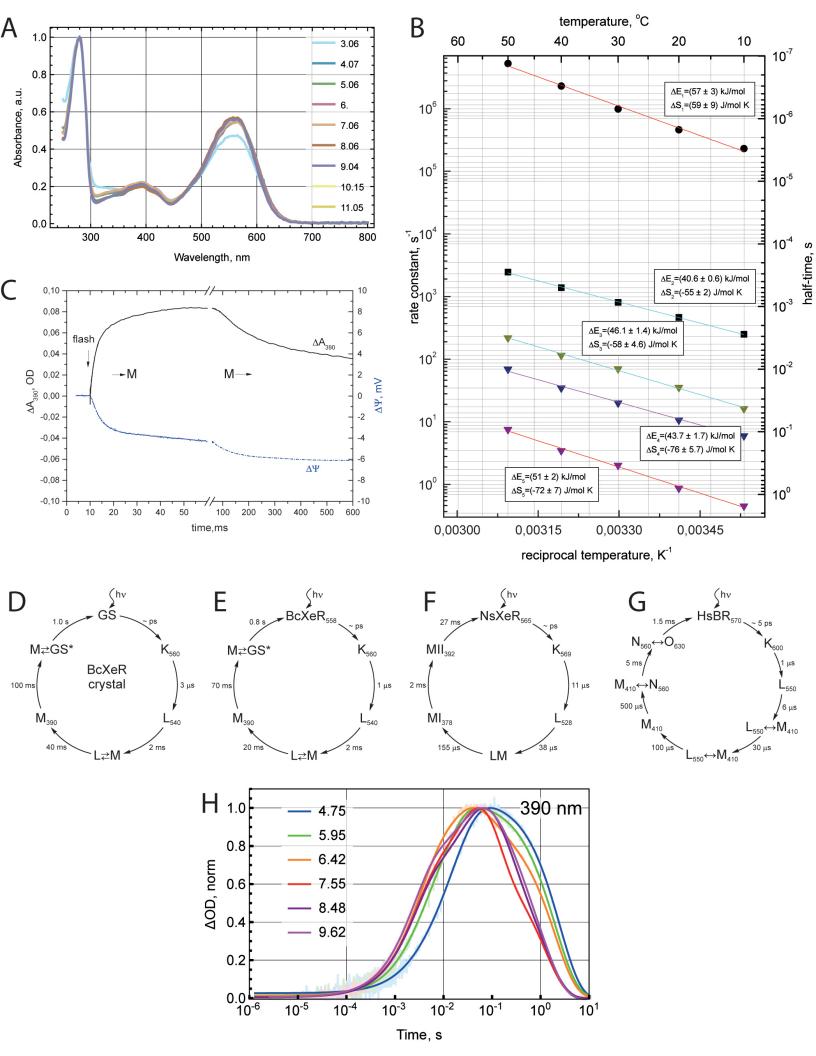




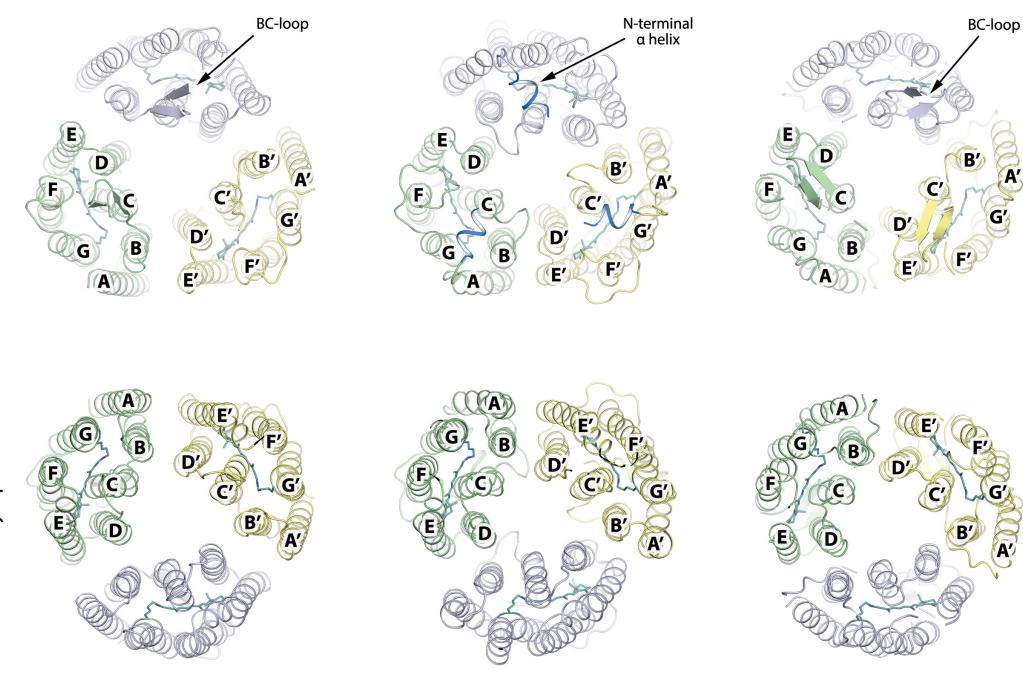
Ground state







BcXeR



NsXeR

HsBR

